A Riemannian Manifold Approach to Constrained Resource Allocation in ISAC

Shayan Zargari, Diluka Galappaththige, *Member, IEEE*, and Chintha Tellambura, *Fellow, IEEE*, H. Vincent Poor, *Life Fellow, IEEE*

***Abstract*—This paper introduces a universal optimization framework for integrated sensing and communication (ISAC) systems, which are expected to be fundamental aspects of sixth-generation networks. In particular, we develop an iterative augmented Lagrangian manifold optimization (IALMO) framework designed to maximize communication sum rate while satisfying sensing beampattern gain targets, users' minimum rate requirements, and base station (BS) transmit power limits. IALMO applies the principles of Riemannian manifold optimization to navigate the complex, non-convex landscape of the resource allocation problem. It efficiently leverages the augmented Lagrangian method to ensure adherence to constraints. Comprehensive numerical results are presented to validate our framework, which illustrates the IALMO method's superior capability to enhance the dual functionalities of communication and sensing in ISAC systems. For instance, with 12 antennas and $30\,\mathrm{dBm}$ BS transmit power, our proposed IALMO algorithm delivers a $4.2\,\%$ sum rate gain over a benchmark optimization-based algorithm.**

Remarkably, the suggested method performs better in complexity and execution time. For instance, the proposed IALMO algorithm reduces average algorithm execution time by $89.5\,\%$ with 20 BS transmit antennas compared to the standard optimization-based benchmark. This work demonstrates significant improvements in system performance and contributes a new algorithmic perspective to ISAC resource management.

***Index Terms*—Integrated sensing and communication, transmit beamforming, manifolds algorithm.**

I. Introduction

The future wireless landscape, encompassing the Internet of Things, vehicle-to-everything, smart traffic control, virtual/augmented reality, smart homes, unmanned aerial vehicles, and factory automation, demands ultra-reliable, low-latency sensing and communication [1]–[5]. This necessitates a shift towards integrated sensing and communication (ISAC), merging traditional communication architectures with advanced sensing capabilities [1]–[5]. Moreover, ISAC can significantly improve spectrum utilization and energy efficiency (EE) and reduce implementation costs by leveraging the dual use of radio signals, hardware architecture, and signal processing for sensing and communication [1]–[5]. On the other hand, recent advances in extremely large-scale antenna arrays and high-frequency communication (i.e., millimeter wave (mmWave) and terahertz (THz)) facilitate high-resolution sensing (in both range and angle) and accuracy (in detection and estimation), achieving the stringent sensing requirements expected for future applications [1]–[5].

S. Zargari, D. Galappaththige, and C. Tellambura with the Department of Electrical and Computer Engineering, University of Alberta, Edmonton, AB, T6G 1H9, Canada (e-mail: {zargari, diluka.lg, ct4}@ualberta.ca).

H. V. Poor is with the Department of Electrical and Computer Engineering, Princeton University, Princeton, NJ 08544 USA (e-mail: poor@princeton.edu).

A. Previous Approaches for Beamforming Design

Many ISAC beamforming designs have recently been developed, each with distinct objectives and optimization methods [6]–[11] (see Table I). In particular, [6] uses zero-forcing (ZF) and semidefinite relaxation (SDR) to maximize the weighted sum of communication and radar rates in a multiple-input multiple-output (MIMO) ISAC system. The study [7] designs base station (BS) beamforming via successive convex approximation (SCA) and SDR-based iterative method to enhance the energy efficiency of the multi-user, multi-target ISAC system. Reference [8] designs transmit and receive beamforming for a single target to maximize sensing signal-to-noise-plus-interference ratio (SINR) and proposes an alternating optimization (AO) algorithm using semidefinite programming (SDP), Charnes-Cooper transformation, and minimum variance distortionless response beamforming. Reference [9] presents ISAC transmit beamforming designs with two design goals: Maximizing the minimum weighted beampattern gain and matching the sensing beam pattern. For both designs, SDR-based optimal solutions are proposed. Study [10] optimizes the BS transmit beamforming and the user transmit power based on the SCA technique for a full-duplex (FD) ISAC system under transmit power minimization and sum-rate maximization.

In [11], a block coordinate descent (BCD) iterative algorithm based on inner approximation (IA) and SDR methods is proposed to jointly optimize snapshot duration, BS beamforming, and artificial noise, in a dual-functional radar-communication (DFRC) system to serve legitimate users while sensing eavesdroppers.

Before exploring the manifold optimization (MO) approach, it is helpful to review conventional techniques for non-convex optimization problems (NCOPs): SDR, SDP, SCA, AO, and BCD. SDR, or semidefinite relaxation, converts non-convex quadratically constrained problems into convex ones, often introducing a non-convex rank-one constraint [16]. To obtain a rank-1 solution, penalty-based methods or Gaussian randomization are used [16]. Despite this, SDR is widely applied in beamforming design and other areas. Another standard method is successive convex approximation (SCA), which tackles NCOPs by iterating a series of convex approximations [17], [18], linearizing or approximating non-convex parts with convex functions based on the current solution. SCA is used in power control, resource allocation, and other wireless problems. Finally, alternating optimization (AO) or block coordinate descent (BCD) decomposes NCOPs into smaller sub-problems, each typically having a closed-form or convex solution. The process alternates between sub-problems until

TABLE I: Comparison of ISAC optimization studies.

Ref.	Strategy	Objectives	Application	Lagrange	Manifold
[6]	SDR	Maximize weighted $\mathcal{R}_c$ and $\mathcal{R}_s$	Multi-user, single target ISAC	✗	✗
[7]	SCA and SDR	Maximize EE	Multi-user, multi-target ISAC	✗	✗
[8]	AO and SDR	Maximize γ_s	Multi-user, single target ISAC	✗	✗
[9]	SDR	Maximize beampattern gain	Multi-user, single target ISAC	✗	✗
[10]	SCA	Minimize P_t and maximize $\mathcal{R}_c$	Multi-user, single target FD ISAC	✗	✗
[11]	IA, SDR, and BCD	Maximize $\mathcal{SR}_c$	Multi-user, single target secure communication in DFRC	✗	✗
[12]	PPCCM	Radar and mutual interference beampattern matching	IRS-aided multi-user, multi-target ISAC	✗	CCM $\times$ CCM
[13]	MO	Minimize weighted communication and radar beamforming errors	Single-user, multi-target mmWave DFRC	✓	CCM
[14]	AO and MO	Maximize $\mathcal{R}_c$	IRS-aided multi-user, single-target RCC	✗	CCM and OM
[15]	MO	Maximize $\mathcal{R}_c$ and γ_s	Multi-user, single target transceiver design for ISAC	✗	CCM $\times$ CSM
This work	MO and ALM	Maximize $\mathcal{R}_c$ subject to sensing beampattern gain and communication SINR	Generic multi-user, multi-target ISAC	✓	CSM

$\mathcal{R}_c$: Communication sum rate, $\mathcal{R}_s$: Sensing rate, γ_s: Sensing SINR, $\mathcal{SR}_c$: Sum secrecy rate, P_t: BS transmit power, OM: Oblique manifold.

convergence, making AO widely used in optimization tasks [19].

B. Riemannian Manifold Optimization

A Riemannian manifold $\mathcal{M}$ is a manifold equipped with a Riemannian metric, which assigns a positive definite inner product to each tangent space, defining notions of distance and angle between tangent vectors at each point [20]. MO naturally applies when optimization parameters are constrained to lie on a manifold, such as the surface of a sphere, the set of rotation matrices, or the space of symmetric positive definite matrices [21]. A basic example of MO is finding the shortest path (geodesic) between two points on a sphere's surface [22]. Here, the sphere is the manifold, and the goal is to minimize the distance function constrained to the surface. Unlike in Euclidean space, where the shortest path is a straight line, on a manifold like a sphere, the shortest path is an arc of a circle.

MO has recently been used for communication/radar system designs [12]–[15], [23]–[27]. These works utilize Riemannian steepest descent, conjugate gradient (CG) descent, and others [28].

MO-based frameworks are developed in [23], [24], [29] to improve communication performance, while [25]–[27] consider MIMO radar systems. Recently, [12]–[15] use MO in ISAC systems. In particular, [12] proposes a parallel product complex circle manifold (PPCCM) framework for an intelligent reflecting surface (IRS)-aided multi-user, multi-target ISAC system. This approach exploits the constant modulus constraints (CMCs) (for BS beamforming and IRS phase shifts) to minimize the beampattern matching error. However, it does not consider the quality-of-service (QoS) for communication and sensing and cannot handle additional constraints. It converts the optimization problem into an unconstrained coupling quadratic problem and develops a parallel CG algorithm. Reference [13] studies a hybrid (i.e., digital and analog) beamforming design for a mmWave system with a single user without considering the QoS for communication and sensing. This approach minimizes the weighted sum of communication and radar beamforming errors by proposing a Riemannian product manifold trust region algorithm. However, it is limited to single-user scenarios and performs identically to a BCD-based conventional solution. Reference [15] proposes a robust transceiver design that jointly optimizes sensing accuracy and communication performance by adjusting the weighting factor between radar and communication over a product complex circle-sphere manifold (PCCSM). However, it does not consider the QoS for communication and sensing, and the global optimality of the method is unclear.

The work in [14] focuses on maximizing the communication sum rate in an IRS-assisted radar and communication coexistence (RCC) system. However, there are key differences between their approach and ours regarding system configuration, algorithm, and constraints. In [14], separate transmitters are used for communication and sensing, whereas this work adopts the ISAC framework that uses a shared infrastructure for both tasks. Additionally, while [14] employs AO over two manifolds, i.e., one for unit-modulus constraints and the other for power constraints, our method uses an augmented Lagrangian method (ALM) on a complex sphere manifold (CSM), which can handle communication SINR and sensing beampattern requirements. Furthermore, the constraints in [14] focus primarily on minimizing communication interference at the radar, while our formulation optimizes communication and maintains sensing performance.

Table I compresses the above discussion, clearly comparing with other works that use MO or not. The table shows significant differences in system design, problem formulation, and algorithmic approach. The essential technical contribution of this work is the integration of MO with the ALM for generic multi-user, multi-target ISAC systems. The details are further explained in the next section.

C. Motivation and Our Contribution

The gaps mentioned above motivate new algorithms to enhance the performance of ISAC systems with multiple users and targets. Thus, this work aims to optimize the BS transmit beamforming to maximize the aggregate communication sum

rate of the users while ensuring sensing beampattern gain targets, minimum rate/SINR requirements for users, and BS transmit power limits. As this problem is non-convex, our approach introduces a new and adaptable ALM-based MO strategy explicitly tailored for optimizing ISAC systems.

The novelty and key contributions of this paper are as follows:

- We develop an iterative augmented Lagrangian manifold optimization (IALMO) algorithm for general ISAC systems. This algorithm maximizes the communication sum rate and satisfies the sensing beampattern gain requirements, users' minimum SINR requirements, and the BS transmit power limit, paving the way for realizing efficient ISAC networks. The algorithm is based on adding a penalty term to the classical Lagrangian approach [28].
- To the best of our knowledge, this is the first study in ISAC to marry a Riemannian MO with an augmented Lagrangian framework, innovatively overcoming the challenges of non-convex optimization endemic to ISAC resource allocation.
- While a few prior works [12], [14], [15] use MO techniques, except [13], they do not consider the iterative refinement of Lagrange multipliers. Conversely, [13] is limited to a single-user scenario in a DFRC system. In contrast, for generic multi-user multi-target ISAC, our proposed algorithm improves these earlier techniques by concurrently updating the Lagrangian and Lagrange multipliers until convergence. This method guarantees the dual fulfillment of communication and sensing requirements, marking a significant advance in ISAC resource management. Importantly, prior methods are confined to limited constraints; our solution approach can handle any constraints, leading to a generalized and universal ISAC framework.
- Numerical experiments show that IALMO outperforms the conventional iterative convex-concave procedure algorithm (CCPA) based on SDR and SCA. Improvements in communication sum rate and significant reductions in execution time are achieved while satisfying the sensing beampattern gain requirements. For example, with 12 antennas and at $30\,\mathrm{dBm}$ of BS power, IALMO delivers an $4.2\,\%$ sum rate gain over CCPA.
- Moreover, dramatic gains are observed in reducing computational and time complexities. For example, IALMO is ten times faster than CCPA for 20 BS transmit antennas (Fig. 5). Moreover, the speed-up factor increases with the number of antennas. This suggests that IALMO scales up while restricting the complexity growth. As ISAC systems adapt to large-scale networks and dense deployment scenarios, IALMO may provide computational and performance gains to meet those needs.

Notation: $\mathbb{C}^{M\times N}$ and $\mathbb{R}^{M\times 1}$ represent $M\times N$ dimensional complex matrices and $M\times 1$ dimensional real vectors, respectively. For a square matrix $\mathbf{A}$, $\mathbf{A}^{\mathrm{H}}$ and $\mathbf{A}^{\mathrm{T}}$ are the Hermitian conjugate transpose and transpose, respectively. $\mathbf{I}_M$ denotes the M-by-M identity matrix. $\mathbf{0}_M$ is the M-dimensional all-zero vector. The Euclidean norm of a complex vector and the absolute value of a complex scalar are denoted by $\|\cdot\|$ and $|\cdot|$, respectively. Expectation and the real part of a complex number are denoted by $\mathbb{E}[\cdot]$ and $\Re(\cdot)$, respectively. $\mathbf{1}_{\{x\}}$ equals 1 if $x>0$ and 0 otherwise. A circularly symmetric complex Gaussian (CSCG) random vector with mean $\boldsymbol{\mu}$ and covariance matrix $\mathbf{C}$ is denoted by $\sim\mathcal{CN}(\boldsymbol{\mu},\,\mathbf{C})$. The operation $\mathrm{unt}(\mathbf{a})=\left[\frac{a_1}{|a_1|},\ldots,\frac{a_n}{|a_n|}\right]$. $\mathbf{A}\circ\mathbf{B}$ is the Hadamard product. Further, $\mathcal{O}$ expresses the big-O notation. The clip operator is defined as $\mathrm{clip}_{[a,b]}(x)=\max\{a,\min(b,x)\}$. Finally, $\mathcal{K}\triangleq\{1,\ldots,K\}$, $\mathcal{N}\triangleq\{1,\ldots,N\}$, and $\mathcal{K}_k\triangleq\mathcal{K}\setminus\{k\}$.

II. System, Channel, and Signal Models

This section describes the ISAC system, channel, and signal model.

A. System and Channel Models

The ISAC system (Fig. 1) comprises an M-antenna BS with uniform linear array (ULA) antennas, K single-antenna communication users, and N targets. The BS antennas are spaced at half-wavelengths [10]. The BS communicates with the users in the downlink and performs radar sensing towards N potential target directions. We also assume that users and targets remain static during a coherence time [10]. However, the algorithms may also apply to mobile scenarios. For example, in vehicular ISAC studies, speeds around $1\,\mathrm{m/s}$ are considered [30]–[32], with channel coherence time depending on mobility speed. To accommodate mobility, the algorithms must run at a frequency that aligns with the mobility speed, ensuring timely updates to channel estimates.

Block flat-fading channels are assumed. In each fading block, $\mathbf{h}_k\in\mathbb{C}^{M\times 1}$ and $\mathbf{a}(\theta_n)\in\mathbb{C}^{M\times 1}$ denote the BS-to-k-th user and the BS-to-n-th target channels, respectively. Here, the pure communication channels are given as

$$\mathbf{h}_k=\zeta_{h_k}^{1/2}\tilde{\mathbf{h}}_k,\ \forall k\in\mathcal{K}, \tag{1}$$

where ζ_{h_k} is the large-scale pathloss, which stays constant for several coherence intervals, and $\tilde{\mathbf{h}}_k\sim\mathcal{CN}(\mathbf{0},\mathbf{I}_M)$ accounts for the small-scale Rayleigh fading.

On the other hand, to model the sensing channels between the BS and the targets, the echo signal representation in MIMO radar systems is assumed [10]. Thus, these channels are modeled as line-of-sight (LoS) channels using transmit array steering vectors to the direction θ_n as [10]:

$$\mathbf{a}(\theta_n)=\frac{1}{\sqrt{M}}\left[1,e^{j\pi\sin(\theta_n)},\ldots,e^{j\pi(M-1)\sin(\theta_n)}\right]^{\mathrm{T}},\ \forall n\in\mathcal{N}, \tag{2}$$

where θ_n is the n-th target's direction with respect to the x-axis of the coordinate system.

Remark 1. *The following assumptions are standard and widely used: (i) $\{\theta_n\}_{n\in\mathcal{N}}$ is assumed to have been pre-estimated known by the BS for beamforming design using past scanning [10], [33], [34], (ii) A separate channel estimation phase is employed before communication and sensing to ensure channel state information (CSI) is available for beamforming design, and (iii) The BS and the user are connected via a control link, exchanging necessary commands [35].*

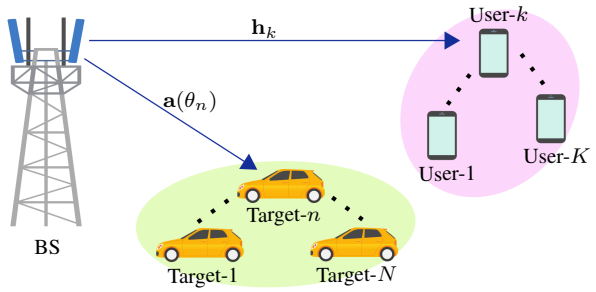

Fig. 1: System model of an ISAC system: A M-antenna BS communicates with K communication users and senses N targets using a shared antenna array.

The ISAC system utilizes the time division duplex (TDD) mode, i.e., separate time slots, for channel estimation and data transfer. Thus, existing and well-developed approaches can be used to estimate CSI [36], [37]. These include the least squares (LS) and minimum mean squared error (MMSE) estimators [36], [37]. The BS and users are thus assumed to have complete knowledge of communication channel CSI, whereas the BS has a general knowledge of the desired beampattern or sensing directions.

B. Transmission Model

The BS transmit signal $\mathbf{x} \in \mathbb{C}^{M\times 1}$ is jointly designed for ISAC [8], [38]. It can be expressed as

$$\mathbf{x} = \sum_{k\in\mathcal{K}} \mathbf{w}_k q_k, \tag{3}$$

where $q_k \in \mathbb{C}$ is the intended data symbol for the k-th user with unit power, i.e., $\mathbb{E}\{|q_k|^2\} = 1$, and $\mathbf{w}_k \in \mathbb{C}^{M\times 1}$ is the BS transmit beamforming vector for the k-th user. Note that $\mathbf{w}_k \in \mathbb{C}^{M\times 1}$ is optimized to generate an effective beampattern toward prospective target directions of interest, resulting in a higher radar receive signal-to-noise ratio (SNR) and improved sensing performance [8], [38], [39]. The received signal at the k-th user is given by

$$y_k = \mathbf{h}_k^{\mathrm{H}}\mathbf{x} + n_k = \mathbf{h}_k^{\mathrm{H}}\mathbf{w}_k q_k + \sum_{i\in\mathcal{K}_k} \mathbf{h}_k^{\mathrm{H}}\mathbf{w}_i q_i + n_k, \ \forall k \in \mathcal{K}, \tag{4}$$

where $n_k \sim \mathcal{CN}(0,\sigma^2)$ is the k-th user's additive white Gaussian noise (AWGN). In (4), it is assumed that the users apply clutter rejection techniques to mitigate the reflected interference from the targets and surrounding environment [40], [41].

Remark 2. *Although separate or dedicated sensing beamforming provides additional degrees of freedom at the BS for sensing, it also produces more interference for communication users who fail to remove sensing signal interference. To address this issue, our proposed system utilizes a single beam for both communication and sensing [8], [38], [39].*

III. Communication and Sensing Performance

This section derives user communication rates and the transmit beampatterns for the targets to evaluate and optimize ISAC.

A. Communication Performance

The users utilize the received signal from the BS to decode their intended data. To this end, from (4), the received SINR at the k-th user can be written as

$$\gamma_k = \frac{|\mathbf{h}_k^{\mathrm{H}}\mathbf{w}_k|^2}{\sum_{i\in\mathcal{K}_k}|\mathbf{h}_k^{\mathrm{H}}\mathbf{w}_i|^2 + \sigma^2}, \ \forall k \in \mathcal{K}. \tag{5}$$

Thus, the rate of the k-th user can be approximated by $\mathcal{R}_k = \log_2(1+\gamma_k)$ for $k \in \mathcal{K}$.

B. Sensing Performance

For MIMO radar signal design in sensing scenarios, the transmit beampattern is the fundamental performance metric [42]. Thus, this study focuses on optimizing it since the appropriate design can improve sensing performance in terms of detection, sensing, or recognition through proper echo wave processing [42]. The transmit beam pattern is the power distribution of the transmit signal relative to the sensing angle $\theta \in [-\pi/2, \pi/2]$. The BS transmits a for both communication and target sensing. The beam pattern gain at a certain angular direction is defined as [7]:

$$\begin{aligned} p(\theta_n) &= \mathbb{E}\{|\mathbf{a}(\theta_n)^{\mathrm{H}}\mathbf{x}|^2\} \\ &= \mathbf{a}(\theta_n)^{\mathrm{H}}\left(\sum_{k\in\mathcal{K}}\mathbf{w}_k\mathbf{w}_k^{\mathrm{H}}\right)\mathbf{a}(\theta_n), \ \forall n \in \mathcal{N}. \end{aligned} \tag{6}$$

The transmit beam pattern depends on the radar target sensing requirements. For example, if the direction of potential targets is unknown, it is a uniformly distributed beam pattern. Conversely, the targets' directions are roughly known, e.g., in target tracking applications, it can be maximized in these potential directions [42].

Remark 3. *ISAC is optimized using two crucial metrics: communication SINR and sensing beampattern gain. The first directly affects symbol detection accuracy and reduces errors, which is critical for communication quality. The success of sensing depends on the beampattern gain, which directly influences the probability of detecting targets. Effective target recognition through transmit beamforming relies on a well-crafted sensing beampattern. Therefore, beampattern gain is the primary indicator of sensing effectiveness in our approach. [42].*

Remark 4. *Note that the sensing operation does not require instantaneous CSI since the sensing beampattern gain incorporates averaging over the transmit signal. Hence, following standard ISAC studies, the long-term statistics of the echo channels are assumed to be known at the BS [10], [33], [43].*

Other measures for assessing sensing performance include the transmit beampattern's mean squared error (MSE) and the sensing rate/SINR [6], [10], [44]. The beampattern MSE minimizes the difference between actual and ideal beampatterns, though it requires knowing the ideal beampattern, which may not be available in practice. Alternatively, the sensing rate/SINR evaluates both transmit and receiver beampatterns, indicating the amount of environmental information gathered

from a target's reflected signal. This method requires full-duplex operation, which can degrade performance due to self-interference. This study uses beampattern gain as the performance metric [7], [42]. Beampattern gain maximizes echo signal strength for a specific target, improving detection probability and parameter estimation. While the focus here is on beamforming design, target parameter estimation is left for future research. Our approach can also be adapted for beampattern MSE and sensing rate/SINR.

IV. Problem Formulation

Next, the ISAC problem formulation is established. Maximizing the users' communication sum rate involves optimizing the BS transmit beamforming. Our objective includes meeting the minimum sensing beampattern gain requirements, minimum communication SINR demands, and adhering to the maximum BS transmit power constraint. The problem is thus formulated as follows:

$$\text{(P1)}: \max_{\{\mathbf{w}_k\}_{k\in\mathcal{K}}} \sum_{k\in\mathcal{K}} \log_2(1+\gamma_k), \tag{7a}$$

$$\text{s.t} \quad p(\theta_n) \geq \Gamma_n^{\text{th}},\ \forall n \in \mathcal{N}, \tag{7b}$$

$$\gamma_k \geq \Gamma_k^{\text{th}},\ \forall k \in \mathcal{K}, \tag{7c}$$

$$\sum_{k\in\mathcal{K}} \|\mathbf{w}_k\|^2 \leq p_{\max}, \tag{7d}$$

where (7b) and (7c) guarantee the sensing beampattern gain and SINR requirement of each target and user, respectively, in which Γ_n^{th} denotes the targeted sensing beampattern gain and Γ_k^{th} indicates the SINR threshold. The feasible sensing/SINR threshold depends on pathloss (node distance), transmit power, number of antennas, and number of targets/users. Thus, any random sensing threshold value cannot be utilized. All of these variables, as well as the application scenario, must be considered while selecting it. In addition, (7d) is the BS transmit power constraint with maximum allowable transmit power $p_{\max}$. This problem formulation aligns with the 6G vision of ISAC [1]–[3].

V. Proposed Solution

This section solves problem (P1) based on fractional programming (FP), MO, and ALM to obtain the optimal BS transmit beamforming vectors [45]. Notably, problem (P1) is non-convex due to the non-convex objective function.

However, the manifold method cannot be directly applied to (P1) as the optimization variable involves $\mathbf{W} = [\mathbf{w}_1, \ldots, \mathbf{w}_K]$. Thus, equivalent transformations are performed on (P1) to handle it with MO. Also, the constraints are applied to the entire matrix $\mathbf{W}$. First, an index matrix is defined as a k-order identity matrix, $\mathbf{E}_k$. This index matrix enables the individual representation of any column from $\mathbf{W}$ by combining $\mathbf{W}$ with the index matrix. Thus, the corresponding reformulation of the problem is presented as

$$\text{(P2)}: \max_{\mathbf{W}} \sum_{k\in\mathcal{K}} \log_2\left(1+\bar{\gamma}_k\right), \tag{8a}$$

$$\text{s.t} \quad \mathbf{a}(\theta_n)^{\mathrm{H}}\mathbf{W}\mathbf{W}^{\mathrm{H}}\mathbf{a}(\theta_n) \geq \Gamma_n^{\text{th}},\ \forall n \in \mathcal{N}, \tag{8b}$$

$$\bar{\gamma}_k \geq \Gamma_k^{\text{th}},\ \forall k \in \mathcal{K}, \tag{8c}$$

$$\text{Tr}(\mathbf{W}\mathbf{W}^{\mathrm{H}}) \leq p_{\max}, \tag{8d}$$

where $\mathbf{E}_{ki}$ denotes the i-th column of $\mathbf{E}_k$ and

$$\bar{\gamma}_k = \frac{|\mathbf{h}_k^{\mathrm{H}}\mathbf{W}\mathbf{E}_{kk}|^2}{\sum_{i\in\mathcal{K}_k}|\mathbf{h}_k^{\mathrm{H}}\mathbf{W}\mathbf{E}_{ki}|^2+\sigma^2},\ \forall k \in \mathcal{K}. \tag{9}$$

Note that $\bar{\gamma}_k$ in (9) is the same as the SINR in (5). As sum-log problems are challenging, the Lagrangian dual transform is utilized to move $\bar{\gamma}_k$ to the outside of $\log_2(1+\bar{\gamma}_k)$. Thereby, it converts the original problem into an equivalent version, in which $\mathbf{W}$ is a solution to (P2) only if it is also a solution to (P3) [46, *Theorem 3*]. In addition, the optimal objective values of these two problems are equal [46]. To this end, μ_k is introduced to replace each SINR term in (8a). Thus, (P2) is reformulated as follows [47]:

$$\text{(P3)}: \max_{\mathbf{W},\boldsymbol{\mu}} f(\mathbf{W},\boldsymbol{\mu}) = \frac{1}{\ln(2)}\sum_{k\in\mathcal{K}}\ln(1+\mu_k) + \frac{1}{\ln(2)}\sum_{k\in\mathcal{K}}\left(-\mu_k + \frac{(1+\mu_k)\bar{\gamma}_k}{1+\bar{\gamma}_k}\right), \tag{10a}$$

$$\text{s.t} \quad \text{(8b)} - \text{(8d)}. \tag{10b}$$

where $\boldsymbol{\mu} = [\mu_1, \ldots, \mu_K]$ is the auxiliary variable vector introduced by FP. The reformulated (P3) can be considered as a two-part optimization problem, i.e., (i) an outer optimization over $\mathbf{W}$ with fixed $\boldsymbol{\mu}$ and (ii) an inner optimization over $\boldsymbol{\mu}$ with fixed $\mathbf{W}$. To solve (P3), we adopt an iterative approach where $\mathbf{W}$ and $\boldsymbol{\mu}$ are optimized alternately until the convergence of the objective function is achieved.

A. Optimization of $\boldsymbol{\mu}$ with Fixed $\mathbf{W}$

In each step of the iterative process, the auxiliary variable $\boldsymbol{\mu}$ is first updated based on the values of $\mathbf{W}$ from the previous iteration. Specifically, $f(\mathbf{W},\boldsymbol{\mu})$ is a concave differentiable function over $\boldsymbol{\mu}$ when $\mathbf{W}$ is held fixed, so $\boldsymbol{\mu}$ can be optimally determined by setting each $\frac{\partial f(\mathbf{W},\boldsymbol{\mu})}{\partial \mu_k}$ to zero. Accordingly, the update rule for $\boldsymbol{\mu}$ is given by [47]

$$\mu_k^* = \bar{\gamma}_k,\ \forall k \in \mathcal{K}. \tag{11}$$

For a given $\boldsymbol{\mu}$, to optimize $\mathbf{W}$, the objective function of (P3) can be simplified as [47] (Remark 5)

$$\text{(P4)}: \max_{\mathbf{W}} \sum_{k\in\mathcal{K}} \frac{\hat{\gamma}_k|\mathbf{h}_k^{\mathrm{H}}\mathbf{W}\mathbf{E}_{kk}|^2}{\sum_{i\in\mathcal{K}}|\mathbf{h}_k^{\mathrm{H}}\mathbf{W}\mathbf{E}_{ki}|^2+\sigma^2}, \tag{12a}$$

$$\text{s.t} \quad \text{(8b)} - \text{(8d)}, \tag{12b}$$

where $\hat{\gamma}_k = 1+\mu_k$ for $k \in \mathcal{K}$. It is emphasized that the final version (P4) and the original problem (P1) are equivalent, and transformations do not degrade performance. The simulation results further support this equivalence.

Remark 5. *The equivalence between (P1) and (P4) is established as follows: To convert (P1) to (P2), we combine all beamforming vectors into a single matrix and employ an identity matrix. Thus, (P2) is identical to (P1). In (P3), substituting optimal $\boldsymbol{\mu}^*$ back in $f(\mathbf{W},\boldsymbol{\mu})$ recovers the original sum-of-logarithms in the objective function in (P2), i.e., $\sum_{k\in\mathcal{K}}\log_2(1+\bar{\gamma}_k)$, exactly. Equivalence is therefore established [46], [47]. For a given $\boldsymbol{\mu}$, the only term that depends on*

$\mathbf{W}$ *in* (10a) *is* $\sum_{k\in\mathcal{K}} \frac{(1+\mu_k)\bar{\gamma}_k}{1+\bar{\gamma}_k}$. *The constant terms can thus be eliminated with respective to* $\mathbf{W}$ *while preserving the original objective [18]. Therefore, the objectives and constraints in (P3) and (P4) are the same, establishing their equivalence. The above equivalences, i.e., (P1) to (P2), (P2) to (P3), and (P3) to (P4), prove the equivalence between the initial problem (P1) and the final version (P4) [18], [46], [47].*

B. Constrained Optimization on a Manifold

Herein, (P4) is solved via MO to obtain the BS transmit beamforming vectors.

1) ***Selecting the Manifold****:* The first step is to choose the correct manifold for (P4). To begin with, the power constraint is normalized such that the total power is constrained by $\text{Tr}(\mathbf{W}\mathbf{W}^{\text{H}}) \leq 1$. A modified matrix $\tilde{\mathbf{W}}$, of columns $\{\tilde{\mathbf{w}}_1, \ldots, \tilde{\mathbf{w}}_K\}$, is introduced to meet the condition $\text{Tr}(\tilde{\mathbf{W}}\tilde{\mathbf{W}}^{\text{H}}) = \text{Tr}(\mathbf{W}\mathbf{W}^{\text{H}}) + ||\mathbf{z}||_2^2 = 1$. Here, each column $\tilde{\mathbf{W}}_k$ is defined as $\tilde{\mathbf{w}}_k = [\mathbf{w}_k^{\text{T}}, z_k]^{\text{T}}$, incorporating an additional element z_k from the auxiliary vector $\mathbf{z} = [z_1, \ldots, z_K]$. This auxiliary vector simplifies power normalization without changing the constraint. Next, a CSM is defined as follows:

$$\mathcal{M} = \left\{ \tilde{\mathbf{W}} \in \mathbb{C}^{(M+1)\times K} \mid \text{Tr}(\tilde{\mathbf{W}}\tilde{\mathbf{W}}^{\text{H}}) = 1 \right\}. \tag{13}$$

Thus, (P4) can be recast as a standard unconstrained optimization problem on manifold $\mathcal{M}$:

$$\text{(P5)}: \min_{\tilde{\mathbf{W}}\in\mathcal{M}} \quad \hat{f}(\tilde{\mathbf{W}}) = -\sum_{k\in\mathcal{K}} \frac{\hat{\gamma}_k |\hat{\mathbf{h}}_k^{\text{H}} \tilde{\mathbf{W}} \mathbf{E}_{kk}|^2}{\sum_{i\in\mathcal{K}} |\hat{\mathbf{h}}_k^{\text{H}} \tilde{\mathbf{W}} \mathbf{E}_{ki}|^2 + \sigma^2}, \tag{14a}$$

$$\text{s.t } \hat{g}_n(\tilde{\mathbf{W}}) = \Gamma_n^{\text{th}} - \hat{\mathbf{a}}(\theta_n)^{\text{H}} \tilde{\mathbf{W}}\tilde{\mathbf{W}}^{\text{H}} \hat{\mathbf{a}}(\theta_n) \leq 0, \ \forall n \in \mathcal{N}, \tag{14b}$$

$$\hat{\Psi}_k(\tilde{\mathbf{W}}) = \Gamma_k^{\text{th}} - \frac{|\hat{\mathbf{h}}_k^{\text{H}} \tilde{\mathbf{W}} \mathbf{E}_{kk}|^2}{\sum_{i\in\mathcal{K}_k} |\hat{\mathbf{h}}_k^{\text{H}} \tilde{\mathbf{W}} \mathbf{E}_{ki}|^2 + \sigma^2} \leq 0, \forall k \in \mathcal{K}, \tag{14c}$$

where $\hat{\mathbf{h}}_k = \sqrt{P}[\mathbf{h}_k, 0]$ and $\hat{\mathbf{a}}(\theta_n) = \sqrt{P}[\mathbf{a}(\theta_n), 0]$ serve to adjust the dimensionality and scaling.

2) ***Dealing with constraints in (P5)****:* In (P5), $\mathcal{M}$ represents a Riemannian manifold, and $\hat{f}(X)$, $\hat{g}_n(X)$, and $\hat{\Psi}_k(X)$ are functions from $\mathcal{M}$ to $\mathbb{R}$ that are twice continuously differentiable. The constraints (14b) and (14c), however, pose a unique challenge, demanding a specialized solution approach. Thus, ALM [48] is utilized to address this. The cost function is expressed as follows:

$$\mathcal{L}_\rho(\tilde{\mathbf{W}}, \boldsymbol{\lambda}, \boldsymbol{\kappa}) = \hat{f}(\tilde{\mathbf{W}}) + \frac{\rho}{2} \left(\sum_{n\in\mathcal{N}} \max\left\{0, \frac{\lambda_n}{\rho} + \hat{g}_n(\tilde{\mathbf{W}})\right\}^2 + \sum_{k\in\mathcal{K}} \max\left\{0, \frac{\kappa_k}{\rho} + \hat{\Psi}_k(\tilde{\mathbf{W}})\right\}^2 \right), \tag{15}$$

where $\rho > 0$ is a penalty parameter and $\boldsymbol{\lambda} \in \mathbb{R}^N$ and $\boldsymbol{\kappa} \in \mathbb{R}^K$ are the Lagrange multiplier vectors with $\{\boldsymbol{\lambda}, \boldsymbol{\kappa}\} \geq 0$. Thus, ρ controls the penalty imposed for violating the constraints of (P5) [48]. Setting ρ too high can introduce numerical instabilities, while a value set too low may fail to penalize constraint violations adequately. Initially, the penalty parameter is set and then adjusted based on improvements in constraint satisfaction. If the improvement surpasses a specific threshold, the penalty remains unchanged; otherwise, it increases to more rigorously enforce constraints. Lagrange multipliers estimate the sensitivity of the objective function to the constraints. They act as correction terms that help achieve convergence to the optimal solution [48]. They are initialized with small positive values and iteratively updated to gradually enforce constraints, aiming for a solution that optimally balances both constraints and objectives. The method alternates between optimizing $\tilde{\mathbf{W}}$ for fixed $\boldsymbol{\lambda}$ and $\boldsymbol{\kappa}$ using the MO method and updating $\boldsymbol{\lambda}$ via a gradient-based rule [48].

This method enhances the classical Lagrangian technique by incorporating a penalty term. Thus, the second right-hand term of (15) is the penalty term. However, instead of penalizing based on the original constraints $\hat{g}_n(\tilde{\mathbf{W}}) \leq 0$ and $\hat{\Psi}_k(\tilde{\mathbf{W}}) \leq 0$, the penalty is based on $\hat{g}_n(\tilde{\mathbf{W}}) + \lambda_n/\rho \leq 0$ and $\hat{\Psi}_k(\tilde{\mathbf{W}}) + \kappa_k/\rho \leq 0$. Here, $\{\lambda_n, \kappa_k\}$ and ρ adjust the constraints, shifting them by λ_n/ρ and κ_k/ρ, respectively, and thus changing the point at which infeasibility is penalized. For more details and examples of this method, the reader is referred to [48, Chapter 4].

Note that $\tilde{\mathbf{W}}$ is always confined to manifold $\mathcal{M}$ during this process. Thus, $\mathcal{L}_\rho(\tilde{\mathbf{W}}, \boldsymbol{\lambda}, \boldsymbol{\kappa})$ is differentiable over $\tilde{\mathbf{W}}$, allowing the ALM framework to be directly applied. This approach is called IALMO [28].

3) ***IALMO algorithm using manifold optimization****:* We now consider the minimization of (15) on $\mathcal{M}$.

To minimize smooth function $\mathcal{L}_\rho(\tilde{\mathbf{W}}, \boldsymbol{\lambda}, \boldsymbol{\kappa}) : \mathcal{M} \to \mathbb{R}$, gradients and Hessians are needed in the Riemannian context. The Riemannian CG (RCG) method adapts the classical CG method [28], [49].

The RCG method computes the Riemannian gradient $\text{grad}_{\tilde{\mathbf{W}}_t} \mathcal{L}_\rho(\tilde{\mathbf{W}}, \boldsymbol{\lambda}, \boldsymbol{\kappa})$ at the current point $\tilde{\mathbf{W}}_t$, which represents the direction of the steepest ascent on $\mathcal{M}$ for the objective function $\mathcal{L}_\rho(\tilde{\mathbf{W}}, \boldsymbol{\lambda}, \boldsymbol{\kappa})$. This gradient is inherently linked to the manifold's metric. It lies within the tangent space $T_{\tilde{\mathbf{W}}_t}\mathcal{M}$, i.e., a vector space consisting of all tangent vectors at point $\tilde{\mathbf{W}}_t$, a linearized local proxy for $\mathcal{M}$ at $\tilde{\mathbf{W}}_t$. The subsequent point $\tilde{\mathbf{W}}_{t+1}$ is determined by applying a retraction mapping $R_{\tilde{\mathbf{W}}_t}$, which smoothly projects a search direction vector $\eta_{\tilde{\mathbf{W}}_t}$ from $T_{\tilde{\mathbf{W}}_t}\mathcal{M}$ onto the manifold, ensuring that the update respects the manifold's geometry. To leverage conjugate directions and maintain the efficacy of previous descent directions, the method utilizes a vector transport function $\mathcal{T}_{\tilde{\mathbf{W}}_t \to \tilde{\mathbf{W}}_{t+1}}$, which coherently transfers the conjugate search direction from the tangent space at $\tilde{\mathbf{W}}_t$ to the tangent space at $\tilde{\mathbf{W}}_{t+1}$. This results in a conjugate direction $\eta_{\tilde{\mathbf{W}}_{t+1}}$ that respects the curvature and intrinsic properties of $\mathcal{M}$.

At any point $\tilde{\mathbf{W}}_t$ on a manifold $\mathcal{M}$, the tangent space $T_{\tilde{\mathbf{W}}_t}\mathcal{M}$ contains all possible directions in which one can move from $\tilde{\mathbf{W}}_t$. For CSM $\mathcal{M}$ (13), the tangent space at $\tilde{\mathbf{W}}_t$ is characterized by the set

$$T_{\tilde{\mathbf{W}}_t}\mathcal{M} = \left\{ \mathbf{c} \in \mathbb{C}^{M+1} \mid \Re\{\mathbf{c} \circ \mathbf{W}_t^*\} = \mathbf{0}_{M+1} \right\}, \tag{16}$$

where $\mathbf{c}$ is a complex vector in $\mathbb{C}^{M+1}$. This space is the collection of orthogonal vectors to $\tilde{\mathbf{W}}_t$ in the sense of the

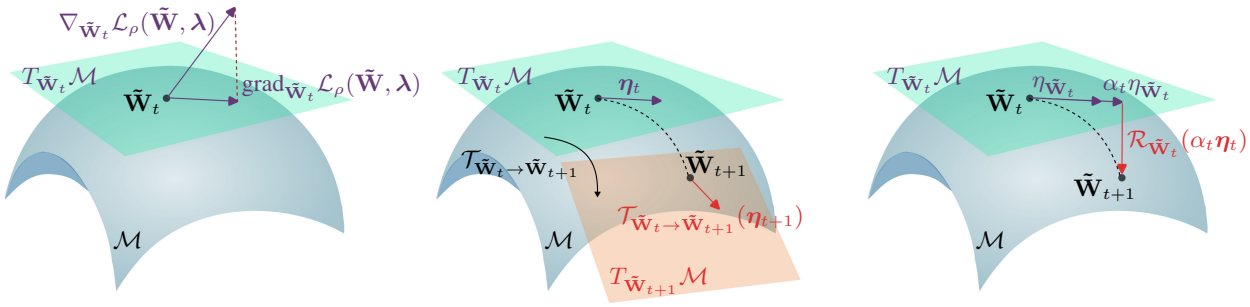

(a) Tangent space and Riemannian gradient (b) Vector transport (c) Retraction

Fig. 2: Key steps in MO.

complex dot product.

Within this tangent space, the vector that represents the steepest ascent of the Lagrangian function, respecting the manifold's geometry, is known as the Riemannian gradient. On the complex circle manifold $\mathcal{M}$, which is a subset of $\mathbb{C}^M$, the Riemannian gradient $\mathrm{grad}_{\tilde{\mathbf{W}}_t}\mathcal{L}_\rho(\tilde{\mathbf{W}},\boldsymbol{\lambda},\boldsymbol{\kappa})$ is the result of orthogonally projecting the standard Euclidean gradient $\nabla_{\tilde{\mathbf{W}}_t}\mathcal{L}_\rho(\tilde{\mathbf{W}},\boldsymbol{\lambda},\boldsymbol{\kappa})$ onto $T_{\tilde{\mathbf{W}}_t}\mathcal{M}$. This projection is visually depicted in Fig. 2a and mathematically expressed as

$$\mathrm{grad}_{\tilde{\mathbf{W}}_t}\mathcal{L}_\rho(\tilde{\mathbf{W}},\boldsymbol{\lambda},\boldsymbol{\kappa}) = \nabla_{\tilde{\mathbf{W}}_t}\mathcal{L}_\rho(\tilde{\mathbf{W}},\boldsymbol{\lambda},\boldsymbol{\kappa}) - \Re\{\nabla_{\tilde{\mathbf{W}}_t}\mathcal{L}_\rho(\tilde{\mathbf{W}},\boldsymbol{\lambda},\boldsymbol{\kappa})\circ\tilde{\mathbf{W}}_t^*\}\circ\tilde{\mathbf{W}}_t, \tag{17}$$

where the Euclidean gradient of (15) is given by (18). Using the Riemannian gradient, Euclidean optimization techniques can be adapted for MO. The CG method's search direction update rule in Euclidean space is given by

$$\boldsymbol{\eta}_{t+1} = -\nabla_{\tilde{\mathbf{W}}_{t+1}}\mathcal{L}_\rho(\tilde{\mathbf{W}},\boldsymbol{\lambda},\boldsymbol{\kappa}) + \beta_t\boldsymbol{\eta}_t, \tag{19}$$

where $\boldsymbol{\eta}_t$ is the current search direction, and β_t is computed using the Hestenes-Stiefel approach [50]. It involves selecting the search direction by combining the steepest descent direction with a previous direction, aiming to minimize the residual. By leveraging conjugacy between search directions, this approach accelerates convergence [50].

However, since $\boldsymbol{\eta}_t$ and $\boldsymbol{\eta}_{t+1}$ belong to different tangent spaces, a process known as vector transport is necessary. This process maps a vector from $T_{\tilde{\mathbf{W}}_t}\mathcal{M}$ to $T_{\tilde{\mathbf{W}}_{t+1}}\mathcal{M}$, respecting the manifold's geometry, as illustrated in Fig. 2b. The transport operation is defined as

$$\mathcal{T}_{\tilde{\mathbf{W}}_t\to\tilde{\mathbf{W}}_{t+1}}(\boldsymbol{\eta}_t) = \boldsymbol{\eta}_t - \Re\{\boldsymbol{\eta}_t\circ\tilde{\mathbf{W}}_{t+1}^*\}\circ\tilde{\mathbf{W}}_{t+1}, \tag{20}$$

and the updated search direction for the CG method on manifolds becomes

$$\boldsymbol{\eta}_{t+1} = -\mathrm{grad}_{\tilde{\mathbf{W}}_{t+1}}\mathcal{L}_\rho(\tilde{\mathbf{W}},\boldsymbol{\lambda},\boldsymbol{\kappa}) + \beta_t\mathcal{T}_{\tilde{\mathbf{W}}_t\to\tilde{\mathbf{W}}_{t+1}}(\boldsymbol{\eta}_t). \tag{21}$$

After the search direction $\boldsymbol{\eta}_t$ is established at $\tilde{\mathbf{W}}_t$, a retraction is employed to map the direction back onto the manifold to find the next point $\tilde{\mathbf{W}}_{t+1}$, as demonstrated in Fig. 2c. The retraction is a smooth mapping, which is defined as

$$\mathcal{R}_{\tilde{\mathbf{W}}_t}(\alpha_t\boldsymbol{\eta}_t) = \mathrm{unt}(\alpha_t\boldsymbol{\eta}_t), \tag{22}$$

where α_t is the step size along the direction $\boldsymbol{\eta}_t$.

Algorithm 1 : Manifold Conjugate Gradient Optimization

1: **Input**: Construct an initial point $\tilde{\mathbf{W}}^{(0)}$, set the convergence tolerance $\delta_1 > 0$, and set $t = 0$.
2: Obtain the Riemannian gradient $\boldsymbol{\eta}_0 = -\mathrm{grad}_{\tilde{\mathbf{W}}_0}\mathcal{L}_\rho(\tilde{\mathbf{W}},\boldsymbol{\lambda},\boldsymbol{\kappa})$ according to (17).
3: **while** $\|\mathrm{grad}_{\tilde{\mathbf{W}}_t}\mathcal{L}_\rho(\tilde{\mathbf{W}},\boldsymbol{\lambda},\boldsymbol{\kappa})\|_2 > \delta_1$ **do**
4: Determine the Armijo backtracking line search step size α_t according to [50].
5: Update $\tilde{\mathbf{W}}_{t+1}$ using retraction $R_{\tilde{\mathbf{W}}_t}(\alpha_t\boldsymbol{\eta}_t)$ as described in (22).
6: Compute the Riemannian gradient at the new point $\mathrm{grad}_{\tilde{\mathbf{W}}_{t+1}}\mathcal{L}_\rho(\tilde{\mathbf{W}},\boldsymbol{\lambda},\boldsymbol{\kappa})$ according to (17).
7: Calculate the vector transport $\mathcal{T}_{\tilde{\mathbf{W}}_t\to\tilde{\mathbf{W}}_{t+1}}(\boldsymbol{\eta}_t)$ using (20).
8: Compute the Hestenes-Stiefel parameter β_t according to [50].
9: Update the CG direction based on (21).
10: $t \leftarrow t+1$
11: **end while**
12: **Output**: $\tilde{\mathbf{W}}^*$.

With these operations, the MO proceeds iteratively and is designed to converge to a critical point of (15), that is, a point where the Riemannian gradient vanishes. Finally, $\tilde{\mathbf{W}}$ can be optimized by applying Algorithm 1 and $\mathbf{W}$ can be obtained via $\mathbf{W} = \tilde{\mathbf{W}}(1:M,K)$.

*4) **Updating Lagrange multipliers**:* After optimizing the optimization variable $\tilde{\mathbf{W}}$ on the Riemannian manifold $\mathcal{M}$, the Lagrange multipliers $\{\boldsymbol{\lambda},\boldsymbol{\kappa}\}$ are updated to reflect progress towards satisfying the constraints. This update incorporates clipping or safeguards to introduce bounds on the multipliers and ensure updates contribute positively towards resolving constraint violations. The updated rules for the Lagrange multipliers at iteration t are given by

$$\lambda_n^{t+1} = \mathrm{clip}_{[\lambda_n^{\min},\lambda_n^{\max}]}\left(\lambda_n^t + \rho_t\hat{g}_n(\tilde{\mathbf{W}}_{t+1})\right),\ \forall n\in\mathcal{N}, \tag{23}$$

$$\kappa_k^{t+1} = \mathrm{clip}_{[\kappa_k^{\min},\kappa_k^{\max}]}\left(\kappa_k^t + \rho_t\hat{\Psi}_k(\tilde{\mathbf{W}}_{t+1})\right),\ \forall k\in\mathcal{K}, \tag{24}$$

Specifically, clipping confines each Lagrange multiplier, $\{\lambda_n^{t+1},\kappa_k^{t+1}\}$, within a specific range determined by minimum and maximum values, denoted as $[\lambda_n^{\min},\lambda_n^{\max}]$ and $[\kappa_n^{\min},\kappa_n^{\max}]$ [28]. This limitation prevents the multipliers from expanding without bounds, ensuring the optimization process

$$\nabla_{\tilde{\mathbf{W}}_t}\mathcal{L}_\rho(\tilde{\mathbf{W}},\boldsymbol{\lambda},\boldsymbol{\kappa})=\sum_{k\in\mathcal{K}}-\hat{\gamma}_k\left(\frac{2\hat{\mathbf{h}}_k^{\mathrm{H}}\tilde{\mathbf{W}}_t\mathbf{E}_{kk}\hat{\mathbf{h}}_k\mathbf{E}_{kk}^{\mathrm{H}}}{\sum_{j\in\mathcal{K}}\left|\hat{\mathbf{h}}_k^{\mathrm{H}}\tilde{\mathbf{W}}_t\mathbf{E}_{kj}\right|^2+\sigma_k^2}-\sum_{i\in\mathcal{K}}\frac{2\left|\hat{\mathbf{h}}_k^{\mathrm{H}}\tilde{\mathbf{W}}_t\mathbf{E}_{kk}\right|^2\hat{\mathbf{h}}_k^{\mathrm{H}}\tilde{\mathbf{W}}_t\mathbf{E}_{ki}\hat{\mathbf{h}}_k\mathbf{E}_{ki}^{\mathrm{H}}}{\left(\sum_{j\in\mathcal{K}}\left|\hat{\mathbf{h}}_k^{\mathrm{H}}\tilde{\mathbf{W}}_t\mathbf{E}_{kj}\right|^2+\sigma_k^2\right)^2}\right)$$
$$-2\rho\sum_{n\in\mathcal{N}}\mathbf{1}_{\left\{\frac{\lambda_n}{\rho}+\hat{g}_n(\tilde{\mathbf{W}})\right\}}\left(\frac{\lambda_n}{\rho}+\hat{g}_n(\tilde{\mathbf{W}})\right)\hat{\mathbf{a}}(\theta_n)\hat{\mathbf{a}}(\theta_n)^{\mathrm{H}}\tilde{\mathbf{W}}-2\rho\sum_{k\in\mathcal{K}}\mathbf{1}_{\left\{\frac{\kappa_k}{\rho}+\hat{\Psi}_k(\tilde{\mathbf{W}})\right\}}\left(\frac{\kappa_k}{\rho}+\hat{\Psi}_k(\tilde{\mathbf{W}})\right)$$
$$\times\left(\frac{2\hat{\mathbf{h}}_k^{\mathrm{H}}\tilde{\mathbf{W}}_t\mathbf{E}_{kk}\hat{\mathbf{h}}_k\mathbf{E}_{kk}^{\mathrm{H}}}{\sum_{j\in\mathcal{K}_k}\left|\hat{\mathbf{h}}_k^{\mathrm{H}}\tilde{\mathbf{W}}_t\mathbf{E}_{kj}\right|^2+\sigma_k^2}-\sum_{i\in\mathcal{K}_k}\frac{2\left|\hat{\mathbf{h}}_k^{\mathrm{H}}\tilde{\mathbf{W}}_t\mathbf{E}_{kk}\right|^2\hat{\mathbf{h}}_k^{\mathrm{H}}\tilde{\mathbf{W}}_t\mathbf{E}_{ki}\hat{\mathbf{h}}_k\mathbf{E}_{ki}^{\mathrm{H}}}{\left(\sum_{j\in\mathcal{K}_k}\left|\hat{\mathbf{h}}_k^{\mathrm{H}}\tilde{\mathbf{W}}_t\mathbf{E}_{kj}\right|^2+\sigma_k^2\right)^2}\right) \tag{18}$$

remains stable and controlled. In addition, the multipliers are only updated if there is a sufficient reduction in the violation of constraints. This approach avoids updating too soon or aggressively, mitigating ill-conditioning effects and instability.

Note that our approach and solution are not restricted to the specific system model in Fig. 1 or the constraints in (P1). It can readily accommodate any ISAC system model, including additional constraints on (P1), offering a more universal solution than previous methods [12]–[14].

The solution process for (P2), named IALMO, is summarized in Algorithm 2. It generates a sequence $\{\epsilon_t\}$ that converges to zero, resulting in a global minimizer for (P2). At each iteration t, it produces a candidate solution $\mathcal{L}_{\rho_t}(\tilde{\mathbf{W}}_{t+1},\boldsymbol{\lambda}_t,\boldsymbol{\kappa}_t)\leq\mathcal{L}_{\rho_t}(\tilde{\mathbf{W}}_t,\boldsymbol{\lambda}_t,\boldsymbol{\kappa}_t)+\epsilon_t$ (Section VI). Thus, this monotonically decreasing nature combined with the upper bound imposed on the objective function assures the convergence. These two factors provide a sufficient condition for establishing that the algorithm will converge. In addition, the core iterative process involves recalculating the transmit beamforming vector, updating the Lagrange multipliers according to whether the constraints are met, and adjusting the penalty value based on the progress toward meeting the accuracy tolerance and constraint conditions. The iteration continues until the solution stabilizes within a defined minimum distance $d_{\min}$ and the accuracy tolerance.

Moreover, the computational complexity of Algorithm 2 is primarily due to the Algorithm 1 iterations. Consequently, the per-iteration complexity is $\mathcal{O}(MK+MK^3)$. Considering T iterations for convergence, the total complexity is approximated as $\mathcal{O}(T(MK^2+NK))$.

Algorithm 2 : IALMO Algorithm

1: **Require**: $\mathcal{M}$, $\hat{f}(\tilde{\mathbf{W}})$, $\{\hat{g}_n(\tilde{\mathbf{W}})\}_{n\in\mathcal{N}}$, $\{\hat{\Psi}_k(\tilde{\mathbf{W}})\}_{k\in\mathcal{K}}$: $\mathcal{M}\to\mathbb{R}$.
2: **Initialization**: Initial candidate $\tilde{\mathbf{W}}_0\in\mathcal{M}$, convergence tolerance $\delta_2>0$, Lagrange multipliers $\boldsymbol{\lambda}^0\in\mathbb{R}^N$, $\boldsymbol{\kappa}^0\in\mathbb{R}^K$, accuracy tolerance $\epsilon_{\min}$, initial accuracy $\epsilon_0>0$, initial penalty factor ρ^0, reduction factors $\theta_\epsilon\in(0,1)$ and $\theta_\rho>1$, boundaries for the multipliers $\lambda_n^{\min},\lambda_n^{\max}\in\mathbb{R}$ and $\kappa_k^{\min},\kappa_k^{\max}\in\mathbb{R}$ ensuring $\lambda_n^{\min}\leq\lambda_n^{\max}$ and $\kappa_k^{\min}\leq\kappa_k^{\max}$, ratio $\tau\in(0,1)$, and minimum acceptable distance $d_{\min}$. Set $t_1=0$.
3: **while** dist$(\hat{f}(\tilde{\mathbf{W}}_{t_1}),\hat{f}(\tilde{\mathbf{W}}_{t_1+1}))\geq\delta_2$ **do**
4: Calculate γ according to the update rule defined in (11).
5: Set $\tilde{\mathbf{W}}_0=\tilde{\mathbf{W}}_{t_1+1}$ and $t=0$.
6: **while** dist$(\tilde{\mathbf{W}}_t,\tilde{\mathbf{W}}_{t+1})\geq d_{\min}$ or $\epsilon_t>\epsilon_{\min}$ **do**
7: Compute the beamforming matrix $\tilde{\mathbf{W}}_{t+1}$ via **Algorithm** 1.
8: Update the Lagrange multipliers using (23) and (24).
9: Set $\sigma_n^{t+1}=\max\left\{\hat{g}_n(\tilde{\mathbf{W}}_{t+1}),-\frac{\lambda_n^{t+1}}{\rho_t}\right\},\forall n$.
10: Set $\tilde{\sigma}_k^{t+1}=\max\left\{\hat{\Psi}_k(\tilde{\mathbf{W}}_{t+1}),-\frac{\kappa_k^{t+1}}{\rho_t}\right\},\forall k$.
11: Adjust the accuracy tolerance $\epsilon_{t+1}=\max\{\epsilon_{\min},\theta_\epsilon\epsilon_t\}$.
12: **if** $t=0$ or $\max\limits_{n,k}\{|\sigma_n^{t+1}|,|\tilde{\sigma}_k^{t+1}|\}\leq\tau\max\limits_{n,k}\{|\sigma_n^t|,|\tilde{\sigma}_k^t|\}$ **then**
13: Maintain the current penalty value: $\rho_{t+1}=\rho_t$.
14: **else**
15: Increment the penalty value: $\rho_{t+1}=\theta_\rho\rho_t$.
16: **end if**
17: $t\leftarrow t+1$;
18: **end while**
19: Update $\tilde{\mathbf{W}}_{t_1+1}=\tilde{\mathbf{W}}_{t+1}$.
20: $t_1\leftarrow t_1+1$;
21: **end while**
22: **Output**: $\mathbf{W}^*=\tilde{\mathbf{W}}_{t_1}^*(1:M,K)$, $\boldsymbol{\lambda}^*$.

VI. Convergence of the IALMO Algorithm

Next, the convergence conditions of the IALMO algorithm for (P5) are analyzed. Specifically, the examination focuses on whether it converges to a global minimizer of (P5), assuming that Algorithm 1 operates with global accuracy.

Proposition 1. *Let the IALMO algorithm be run with $\epsilon_{\min}=0$, generating an infinite sequence $\{\epsilon_t\}$ converging to zero. At each iteration t, let Algorithm 1 identify a candidate solution $\tilde{\mathbf{W}}_{t+1}$ that meets the following condition:*

$$\mathcal{L}_{\rho_t}(\tilde{\mathbf{W}}_{t+1},\boldsymbol{\lambda}_t,\boldsymbol{\kappa}_t)\leq\mathcal{L}_{\rho_t}(\tilde{\mathbf{W}}_t,\boldsymbol{\lambda}_t,\boldsymbol{\kappa}_t)+\epsilon_t, \tag{25}$$

where $\tilde{\mathbf{W}}_{t+1}$ denotes a feasible global minimizer of (P5). If there exists a limit point $\tilde{\mathbf{W}}^*$ within the sequence $\{\tilde{\mathbf{W}}_t\}_{t=0}^{\infty}$ produced by the ALMO algorithm, then $\tilde{\mathbf{W}}^*$ also represents a global minimizer of (P5).

Proof. The convergence to a global minimizer can be established by employing the results from Theorem 1 and Theorem 2 in [51], which indicate that the limit point of the sequence generated by IALMO satisfies the global optimality criteria

for (P5). In the following, we also provide a detailed outline of the proof.

1) Non-increasing sequence and boundedness: Given the condition

$$\mathcal{L}_{\rho_t}(\tilde{\mathbf{W}}_{t+1}, \boldsymbol{\lambda}_t, \boldsymbol{\kappa}_t) \leq \mathcal{L}_{\rho_t}(\tilde{\mathbf{W}}_t, \boldsymbol{\lambda}_t, \boldsymbol{\kappa}_t) + \epsilon_t, \tag{26}$$

and the fact that $\epsilon_t \to 0$, we have

$$\mathcal{L}_{\rho_t}(\tilde{\mathbf{W}}_{t+1}, \boldsymbol{\lambda}_t, \boldsymbol{\kappa}_t) \leq \mathcal{L}_{\rho_t}(\tilde{\mathbf{W}}_t, \boldsymbol{\lambda}_t, \boldsymbol{\kappa}_t). \tag{27}$$

This implies that the sequence $\{\mathcal{L}_{\rho_t}(\tilde{\mathbf{W}}_t, \boldsymbol{\lambda}_t, \boldsymbol{\kappa}_t)\}$ is non-increasing and bounded below by the global minimum of the Lagrangian function. Therefore, it converges to some limit L^*.

2) Existence of a limit point: Let $\tilde{\mathbf{W}}^*$ be a limit point of the sequence $\{\tilde{\mathbf{W}}_t\}_{t=1}^T$. By the Bolzano-Weierstrass theorem, every bounded sequence in $\mathbb{R}^T$ has a convergent subsequence [52]. Thus, there exists a subsequence $\{\tilde{\mathbf{W}}_t\}_{t=1}^T$ such that $\{\tilde{\mathbf{W}}_t\}_{t=1}^T \to \tilde{\mathbf{W}}^*$.

3) Feasibility of $\tilde{\mathbf{W}}^*$: To show that $\tilde{\mathbf{W}}^*$ is feasible for the original problem (P5), consider the following arguments. Since the augmented Lagrangian function includes penalty terms for constraint violations, a minimizer of $\mathcal{L}_\rho(\mathbf{W}, \boldsymbol{\lambda}, \boldsymbol{\kappa})$ should drive these violations to zero. Specifically, since the sequence $\{\tilde{\mathbf{W}}_t\}_{t=1}^T$ is generated such that $\mathcal{L}_{\rho_t}(\tilde{\mathbf{W}}_t, \boldsymbol{\lambda}_t, \boldsymbol{\kappa}_t)$ is non-increasing and converges, the penalty terms must also converge to zero to avoid an unbounded increase in the augmented Lagrangian. Thus, one has

$$\begin{aligned}
&\lim_{t\to\infty} \sum_n \max\left\{0, \frac{\lambda_n^t}{\rho_t} + \hat{g}_n(\tilde{\mathbf{W}}_{t+1})\right\} = 0, \\
&\lim_{t\to\infty} \sum_k \max\left\{0, \frac{\kappa_k^t}{\rho_t} + \hat{\Psi}_k(\tilde{\mathbf{W}}_{t+1}\right\} = 0.
\end{aligned} \tag{28}$$

This implies that $\hat{g}_n(\tilde{\mathbf{W}}^*) \leq 0$ and $\hat{\Psi}_k(\tilde{\mathbf{W}}^*) \leq 0$, proving that $\tilde{\mathbf{W}}^*$ is feasible for (P5).

4) Global optimality of $\tilde{\mathbf{W}}^*$: To establish the global optimality of $\tilde{\mathbf{W}}^*$, it is needed to show that $f(\tilde{\mathbf{W}}^*) \leq f(\mathbf{W})$ for any feasible $\mathbf{W}$. Given the condition in the proposition and since $\epsilon_t \to 0$, one has

$$\mathcal{L}_{\rho_t}(\tilde{\mathbf{W}}_{t+1}, \boldsymbol{\lambda}_t, \boldsymbol{\kappa}_t) \leq \mathcal{L}_{\rho_t}(\tilde{\mathbf{W}}_t, \boldsymbol{\lambda}_t, \boldsymbol{\kappa}_t). \tag{29}$$

As $\tilde{\mathbf{W}}_t \to \tilde{\mathbf{W}}^*$, it also follows that $\tilde{\mathbf{W}}_{t+1} \to \tilde{\mathbf{W}}^*$. Consider any feasible point $\mathbf{W}$ for (P5). For large enough t, since $\tilde{\mathbf{W}}_t \to \tilde{\mathbf{W}}^*$ and the penalty terms vanish at feasibility, one has

$$\mathcal{L}_{\rho_t}(\tilde{\mathbf{W}}^*, \boldsymbol{\lambda}_t, \boldsymbol{\kappa}_t) \approx f(\tilde{\mathbf{W}}^*) \quad \text{and} \quad \mathcal{L}_{\rho_t}(\mathbf{W}, \boldsymbol{\lambda}_t, \boldsymbol{\kappa}_t) \approx f(\mathbf{W}). \tag{30}$$

Thus, $f(\tilde{\mathbf{W}}^*) \leq f(\mathbf{W})$, for all feasible $\mathbf{W}$. Therefore, the limit point $\tilde{\mathbf{W}}^*$ of the sequence $\{\tilde{\mathbf{W}}_t\}_{t=1}^T$ generated by the IALMO algorithm is indeed a global minimizer of (P5). This completes the proof of Proposition 1. □

While global optimality may be challenging, convergence to stationary points can often be ensured. The following proposition addresses the first-order convergence scenario.

Proposition 2. *Given the IALMO algorithm with $\epsilon_{\min} = 0$, if at each iteration t, the Algorithm 1 provides a point $\tilde{\mathbf{W}}_{t+1}$ satisfying*

$$\left\|\mathrm{grad}_{\tilde{\mathbf{W}}} \mathcal{L}_{\rho_t}(\tilde{\mathbf{W}}_{t+1}, \boldsymbol{\lambda}_t, \boldsymbol{\kappa}_t)\right\| \leq \epsilon_t, \tag{31}$$

TABLE II: Simulation and algorithm parameters.

Parameter	Value	Parameter	Value
σ^2	$-110\,\mathrm{dB}$	Γ_n^{th}	$-20\,\mathrm{dB}$
M	16	$p_{\max}$	$0\,\mathrm{dBW}$
K	2	δ_1, δ_2	10^{-6}
N	4	ν	2
$d_{\min}$	10^{-10}	ϵ_0	10^{-3}
$\epsilon_{\min}$	10^{-6}	τ	0.5
θ_ϵ	0.5	θ_ρ	0.25
ρ	1	$\{\lambda_n^{\min}, \lambda_n^{\max}\}$	{0,100}

and the sequence $\{\tilde{\mathbf{W}}_t\}_{t=0}^\infty$ has a limit point $\tilde{\mathbf{W}}^*$ within the feasible set of (P2), then $\tilde{\mathbf{W}}^*$ satisfies the Karush-Kuhn-Tucker (KKT) conditions of (P5).

Proof. The proof can be found in [28, *Proposition 3.2*]. More specifically, at the initial iteration ($t = 0$), consider a feasible point $\tilde{\mathbf{W}}_0 \in \mathcal{M}$ and a set of Lagrange multipliers $\boldsymbol{\lambda}^0 \in \mathbb{R}^N$, $\boldsymbol{\kappa}^0 \in \mathbb{R}^K$. Assume the algorithm converges up to iteration t. This implies that $\tilde{\mathbf{W}}_t$ is a stationary point of the Lagrangian function associated with the current set of multipliers $\boldsymbol{\lambda}^t$ and penalty parameters $\{\rho_t\}$. Specifically, given that $\epsilon_{\min} = 0$ and $\epsilon_t \to 0$ as $t \to \infty$, it follows that

$$\left\|\mathrm{grad}_{\tilde{\mathbf{W}}} \mathcal{L}_{\rho_t}(\tilde{\mathbf{W}}_{t+1}, \boldsymbol{\lambda}_t, \boldsymbol{\kappa}_t)\right\| \to 0 \text{ as } t \to \infty. \tag{32}$$

By the continuity of the gradient operator and the Lagrangian function, it follows that $\mathrm{grad}_{\tilde{\mathbf{W}}} \mathcal{L}_{\rho^*}(\tilde{\mathbf{W}}^*, \boldsymbol{\lambda}^*, \boldsymbol{\kappa}^*) = 0$, where $\rho^* = \lim_{t\to\infty} \rho_t$, $\boldsymbol{\lambda}^* = \lim_{t\to\infty} \boldsymbol{\lambda}_t$, and $\boldsymbol{\kappa}^* = \lim_{t\to\infty} \boldsymbol{\kappa}_t$. Since $\tilde{\mathbf{W}}^*$ is within the feasible set of (P2), it satisfies the primal feasibility conditions. The dual feasibility and complementary slackness conditions follow from the properties of the Lagrange multipliers $\{\boldsymbol{\lambda}^*, \boldsymbol{\kappa}^*\}$ [28]. Therefore, $\tilde{\mathbf{W}}^*$ satisfies the KKT conditions of (P5), completing the proof.

Considering $t-1$ iteration, the update of the Lagrange multipliers using (23) guarantees that $\mathcal{L}_\rho(\tilde{\mathbf{W}}, \boldsymbol{\lambda}, \boldsymbol{\kappa})$ remains bounded below since the penalty terms associated with constraint violations are non-negative. The multipliers are clipped within the bounds $\lambda_n^{\min} \leq \lambda_n^{\max}$ and $\kappa_n^{\min} \leq \kappa_n^{\max}$. By the properties of the Riemannian gradient and the assumption that the manifold $\mathcal{M}$ is compact, the sequence $\{\tilde{\mathbf{W}}_t\}_{t=0}^\infty$ lies in a compact subset of $\mathcal{M}$ and therefore has a convergent subsequence. Let $\tilde{\mathbf{W}}^*$ be the limit of this subsequence. Due to the continuity of $\hat{f}(\tilde{\mathbf{W}})$, $\hat{g}_n(\tilde{\mathbf{W}})$, and $\hat{\Psi}_k(\tilde{\mathbf{W}})$, we have that $\tilde{\mathbf{W}}^*$ is a stationary point of $\mathcal{L}_\rho(\tilde{\mathbf{W}}, \boldsymbol{\lambda}, \boldsymbol{\kappa})$. Furthermore, the algorithmic rule that adjusts the penalty parameters $\{\rho_t\}$ in step 12 of Algorithm 2 ensures that, in the limit, constraint violations are penalized sufficiently. This implies that any limit point of the sequence $\{\tilde{\mathbf{W}}_t\}_{t=0}^\infty$ must satisfy the constraints, making $\tilde{\mathbf{W}}^*$ a feasible point of the original problem. Thus, by the first-order optimality conditions on Riemannian manifolds and the properties of the ALM, we conclude that the sequence $\{\tilde{\mathbf{W}}_t\}_{t=0}^\infty$ converges to a stationary point of $\mathcal{L}_\rho(\tilde{\mathbf{W}}, \boldsymbol{\lambda}, \boldsymbol{\kappa})$. □

VII. Simulation Results

Next, simulation results are presented to evaluate the efficacy of the proposed IALMO algorithm.

A. Simulation Setup and Parameters

These are the configurations and parameters used in our simulations. Unless otherwise stated, the simulation parame-

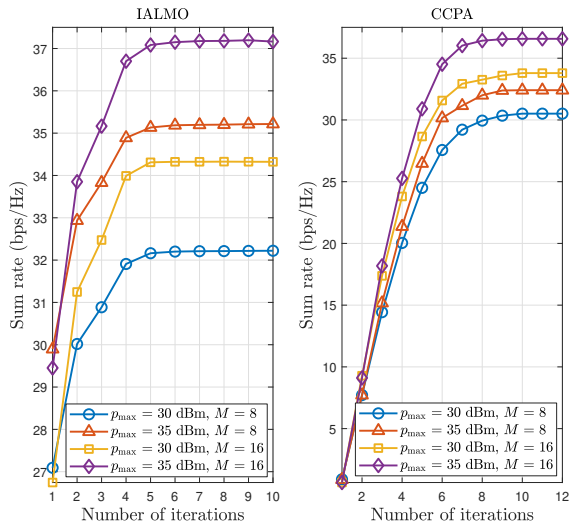

Fig. 3: Convergence rate under different system setups.

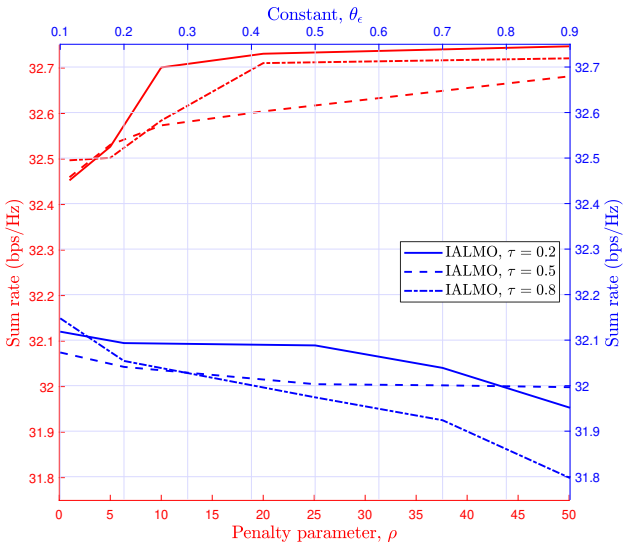

Fig. 4: Sum rate versus penalty parameter ρ (bottom x-axis) and constant θ_ϵ (top x-axis) for the IALMO algorithm, differentiated by line style for each τ setting.

ters are given in Table II [7], [8], [10], [28]. Furthermore, the pathloss model is given by $L(d) = C_0 \left(\frac{d}{D_0}\right)^{-\nu}$, where $C_0 = -30\,\text{dB}$ represents the pathloss at the reference distance $D_0 = 1\,\text{m}$, d represents the individual link distance, and ν denotes the pathloss exponent. To establish a centralized communication point, the BS is positioned at coordinates $\{0, 0\}$. The users are randomly distributed within circular regions centered at $\{50, 30\}$ with a radius of $20\,\text{m}$. Users are positioned at angles of $-30°$ and $30°$ while the sensing directions from the BS are set at $-54°$, $-18°$, $18°$, and $54°$, covering a wide angular range. The simulation consists of 10^3 Monte Carlo trials. In addition, the circles in the figures represent communication users while the triangles denote sensors.

B. Benchmark Schemes

MMSE and ZF beamformers are widely used due to their computational simplicity and effective interference management capabilities [36].

1) *ZF beamforming:* This beamformer considers the communication users only and is denoted as $\mathbf{W}_{\text{ZF}} = \mathbf{H}(\mathbf{H}^{\text{H}}\mathbf{H})^{-1}$, where $\mathbf{H} \in \mathbb{C}^{M\times K}$ represent the channel matrix that contains the channel vectors of all communication users, with the k-th column vector denoted as $\mathbf{h}_k$ for $k \in \mathcal{K}$. The ZF beamformer completely nullifies the interference at non-targeted users. However, this approach completely ignores the sensing targets, and the beamforming matrix depends inversely on the channel matrix. While ZF beamforming eliminates inter-user, its performance degrades in low-SNR conditions.

2) *MMSE beamforming:* This beamforming technique is designed to minimize the total mean squared error (MSE) between the estimated and the actual communication user signals. The MMSE beamforming matrix is given by $\mathbf{W}_{\text{MMSE}} = \mathbf{H}\left(\mathbf{H}^{\text{H}}\mathbf{H} + \sigma^2\mathbf{I}_K\right)^{-1}$. This approach also ignores the presence of sensing targets. It is designed to mitigate interference and optimally balance the signal of interest and the noise. As a result, it can enhance communication performance in moderate to low SNR scenarios.

3) *CCPA Method:* This benchmark utilizes standard optimization techniques such as SDR and SCA, which is equivalent to algorithms in [7]. Thus, it solves (P1) using an iterative CCPA based on SDR and SCA [7]. In particular, by defining $\mathbf{W}_k = \mathbf{w}_k\mathbf{w}_k^{\text{H}}$ and exploiting that $\mathbf{W}_k$ is semidefinite with $\text{Rank}(\mathbf{W}_k) = 1$, (P1) is reformulated as a conventional SDP by relaxing the rank one constraint [53]. The SDP problem is solved using the CVX tool [18]. Finally, to impose the relaxed rank one constraint, Gaussian randomization is utilized [53].

C. Convergence Rate of Algorithm 2

Fig. 3 investigates the convergence of IALMO and CCPA algorithms, illustrating the impact of transmit power and antenna count on the average sum rate across iterations. Notably, $0\,\text{dBW}$ to $5\,\text{dBW}$ power increase, coupled with an expansion from 8 to 16 antenna elements, significantly improves the average sum rate for both schemes, exploiting the increased spatial degrees of freedom. Both algorithms converge to a steady sum rate as the number of iterations increases. However, IALMO achieves faster convergence than CCPA. For instance, in IALMO, the average sum rate rapidly increases within 5 iterations and plateaus after that, regardless of system parameters. In contrast, CCPA requires at least 10 iterations. This indicates a rapid convergence and verifies the efficacy of IALMO.

D. Tuning IALMO Algorithm Parameters

Fig. 4 illustrates the IALMO performance across varying penalty parameter values ρ and constant, θ_ϵ. Three curves represent the sum rate for τ values of 0.2, 0.5, and 0.8.

Specifically, when $\tau = 0.2$, a gradual increase is demonstrated in the sum rate as ρ increases, plateauing beyond a certain point. In contrast, $\tau = 0.5$ and $\tau = 0.8$ initially exhibit a steep ascent, followed by a plateau and then a

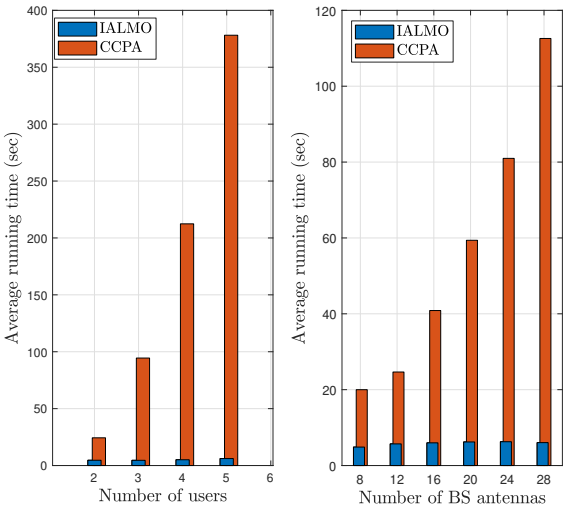

Fig. 5: Average IALMO and CCPA running time versus number of users and BS antennas.

slight decline, suggesting an effective range of ρ for these particular τ values. The choice of these variables - τ, θ_ϵ, and ρ - is motivated by their influence on the convergence and performance of the IALMO algorithm. The ratio τ is critical in updating the Lagrange multipliers, affecting the tightness of constraint satisfaction. Meanwhile, the penalty parameter ρ influences the trade-off between the sum rate's convergence speed and the precision of reaching a feasible solution. The parameters, including the reduction factors θ_ρ and θ_ϵ, and the Lagrange multiplier boundaries $\lambda_{\max}$ and $\lambda_{\min}$, are also carefully selected to strike a balance between algorithmic accuracy and computational efficiency, ultimately optimizing the ISAC system's performance.

E. Average Running Time

Fig. 5 compares the average running times (or computational demand) of IALMO and CCPA. These data are from Matlab simulations for an Intel® Xeon® CPU, clocking at 3.5 GHz. From the left-hand graph with $M = 20$, it can be observed that as the number of users increases from 2 to 10, the average running time for both algorithms also increases. However, the IALMO algorithm has a significantly lower algorithm execution time compared to CCPA, showing a lower computational demand and high efficiency across all user counts.

The right-hand graph compares the two algorithms as the number of BS antennas increases from 8 to 28. Similar to the trend in user count, the average running time for both algorithms increases with the number of BS antennas. Nevertheless, the IALMO algorithm remarkably outperforms CCPA, yielding a lower average running time regardless of the number of BS antennas. For instance, with $M = 20$, the IALMO algorithm achieves 89.5 % reduction in average running time compared to the CCPA. The fundamental reason is that IALMO converts the non-convex problem directly into an MO problem, eliminating the need for approximations. It also combines all beamforming vectors into a single variable to

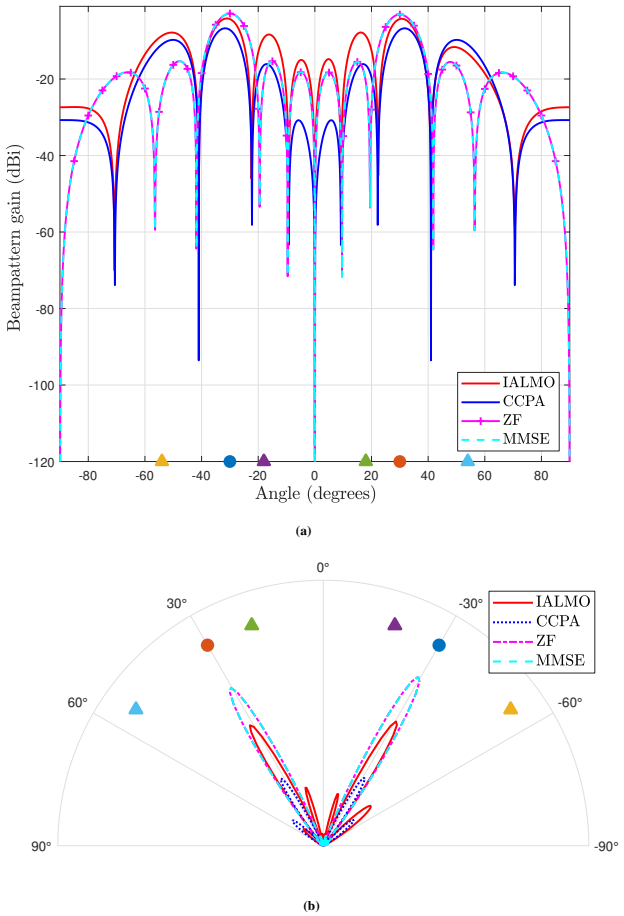

Fig. 6: Beamforming gain comparison with $M = 12$. (a) Directional gain profiles for various algorithms across a $\pm 90^\circ$ angular spread. (b) Polar plot of beam patterns, showcasing the directional gains and sidelobe structure for each method.

efficiently manage large-scale challenges. Conversely, because the CCPA is an iterative process with the computational intensity of the SCA-SDR approximation/relaxation, it requires more resources as the number of users or the antenna array grows, resulting in a long execution time. Furthermore, the exact execution time is mostly determined by the hardware and computing power of the BS, which includes dedicated processing hardware. Hence, run times will be considerably lower than in Fig. 5, potentially much less than the channel coherence time.

F. Beampattern Gains

Fig. 6 presents a comparison of beamforming gains utilizing an array of $M = 12$ antennas at the BS for a set of various algorithms. Specifically, in Fig. 6a, the directional gain profiles are plotted to evaluate the performance of various beamforming approaches. This analysis highlights each algorithm's efficacy in concentrating radiated power in targeted directions, essential for optimizing spatial filtering and minimizing interference. The acuteness of the main lobe peaks directly correlates with the directive gain, which indicates an algorithm's precision in steering the beam. Conversely, the depth of the troughs in the gain profiles indicates the algorithms' ability to reduce signal reception from non-targeted

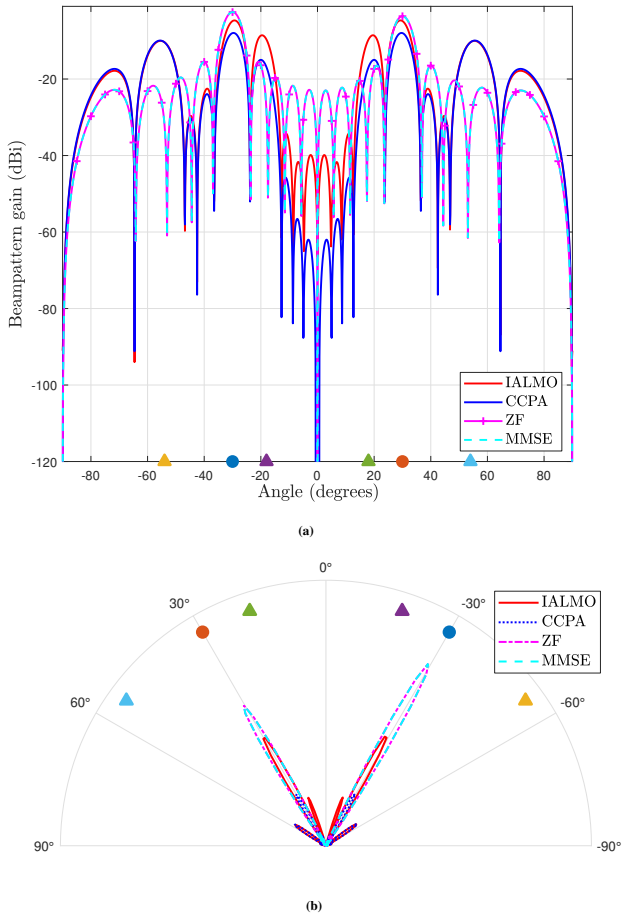

Fig. 7: Beamforming gain comparison with $M = 20$. (a) Directional gain profiles for various algorithms across a $\pm 90^\circ$ angular spread. (b) Polar plot of beam patterns, showcasing the directional gains and sidelobe structure for each method.

directions. This is noticeable through the attenuation levels in the sidelobes. The polar plot in Fig. 6b complements the line graph by mapping the beam patterns onto a polar coordinate system, thus providing an intuitive view of the angular spread and sidelobe structure. The polar representation visualizes the beamwidth and sidelobe suppression capabilities of methods. For instance, a narrower main lobe with lower sidelobes corresponds to a more focused beam with less potential for sidelobe interference.

Fig. 7 extends this comparison to a larger antenna array with $M = 20$ elements. The increase in the number of antenna elements is observed to enhance the directivity and gain of the beam patterns, as demonstrated by the tighter main lobes and increased suppression of sidelobes. This is particularly evident when comparing the polar plots between Figs. 7b and 6b, where the beams are noticeably more focused with higher element count, demonstrating the theoretical beamforming gain improvement with larger arrays.

The IALMO algorithm displays a consistently high level of directivity across both figures. Increasing M results in sharper main lobe peaks and more pronounced sidelobe suppression, thus underscoring an improved spatial filtering efficacy. The CCPA, although showing heightened directivity with array size amplification, marginally underperforms compared to the manifold approach in terms of peak gain acuteness and sidelobe damping. In contrast, while the ZF and MMSE algorithms exhibit increased directivity towards user positions, they present broader main lobes than the IALMO algorithm.

Fig. 8 offers a detailed visualization of the spatial gain profiles achieved by different beamforming algorithms for $M = 20$ antennas. Each figure depicts the gain distribution, employing a color gradient to convey the magnitude of the beamforming gain intuitively. The color intensity indicates the gain strength, e.g., reds indicate higher gains, thus representing areas of focused energy emission. In contrast, blues represent regions of minimal radiated power, indicative of gain troughs or nulls.

For IALMO and CCPA, the plots exhibit multiple, narrowly focused high-gain regions, reflecting the algorithms' capability of generating sharp, directive beams toward targets and users while minimizing interference to and from other directions. Such beam sharpness is particularly advantageous in dense user/target environments where the precision of beam steering is paramount. As observed, IALMO creates sharper beam gains toward users and targets than CCPA. The ZF and MMSE algorithms demonstrate a distinct beam pattern with directive beams only toward users. This implies that ZF and MMSE beamforming are effective for communication but not sensing in ISAC.

Fig. 9 outlines the beampattern gains achieved by IALMO and CCPA under different sensing targets. Furthermore, the horizontal dash-dot lines represent the sensing thresholds. Both algorithms successfully exceed the thresholds in the target directions.

IALMO exhibits a consistent pattern at both power levels, indicating its robust beamforming ability across a diverse power range. A comparison between $-10\,\mathrm{dB}$ and $-20\,\mathrm{dB}$ sensing thresholds reveals that higher power thresholds lead to sharper peaks for targets, indicating a more concentrated energy focus and improved sidelobe suppression. The CCPA, while demonstrating a similar trend in gain enhancement with increased power levels, shows a slightly different pattern. The gain curves suggest that CCPA may provide broader coverage at the cost of less directivity compared to the IALMO algorithm. This characteristic becomes particularly pronounced at the $-10\,\mathrm{dB}$ sensing threshold, where it can be observed that the main lobes are less peaked, implying a trade-off that favors a wider beam spread over pinpoint accuracy.

G. Sum Rate Versus Transmit Power

Fig. 10 illustrates the relationship between the sum rate and the BS transmit power, $p_{\max}$, for $M = 16$. All algorithms consistently increase the sum rate as transmit power increases, underscoring their ability to improve overall system throughput. The ZF and MMSE algorithms have identical performance metrics across the evaluated power range, achieving the highest sum rate. Conversely, the proposed IALMO algorithm outperforms the state-of-the-art CCPA method in terms of sum rate. For instance, at $2\,\mathrm{dBW}$ transmit power, IALMO outperforms the CCPA by $4.3\,\%$ in sum rate. Although ZF and MMSE beamforming achieve higher communication rates

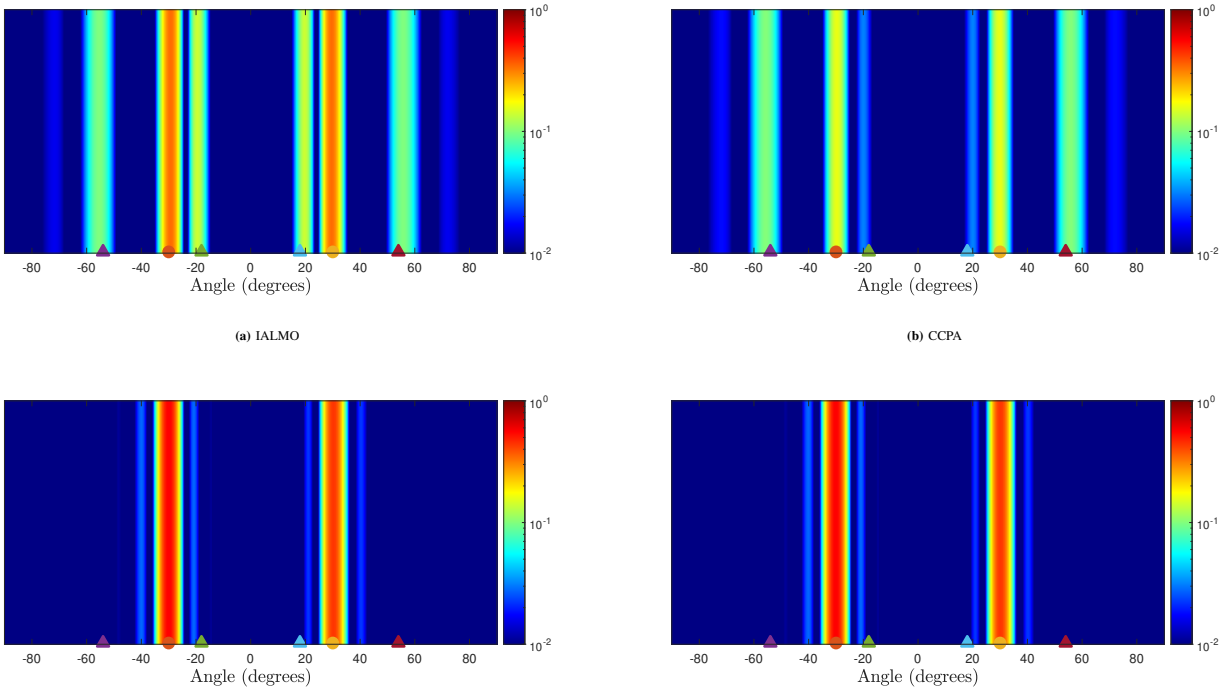

(a) IALMO (b) CCPA (c) MMSE (d) ZF

Fig. 8: Beam pattern gain profiles for various algorithms with $M = 20$, illustrating the gain variations and directivity in a color-coded scale. The intensity of each color reflects the strength of the beamforming gain, with red indicating higher gains and blue indicating lower gains.

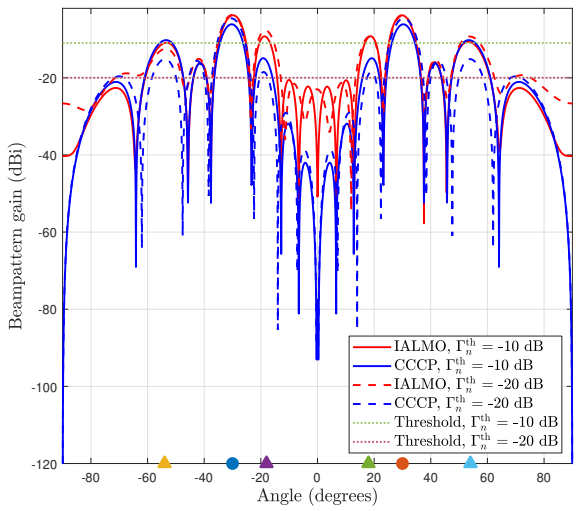

Fig. 9: Beamforming performance for IALMO and CCPA at different targeted sensing beampattern gains with $p_{\max} = 5\,\text{dBW}$.

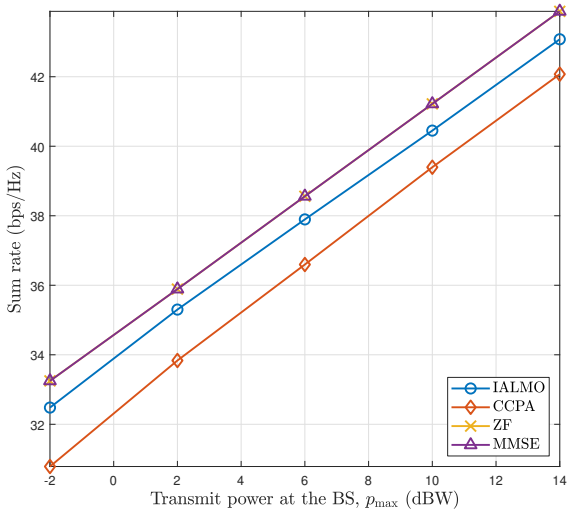

Fig. 10: sum rate versus the transmit power at the BS, $p_{\max}$, for various algorithms.

than IALMO, they do not consider sensing targets. Thus, they cannot detect targets in ISAC systems (see Fig. 8). This suggests that IALMO is more power-efficient, achieving higher throughput gains (i.e., communication and sensing) per unit of power increase.

H. Sum Rate Versus Number of BS Antenna

Fig. 11 compares the sum rate of various algorithms for different numbers of BS antennas, M, for $p_{\max} = 0\,\text{dBW}$. A higher number of BS antennas correlates with an increased sum rate for all algorithms. Thus, they can effectively leverage the spatial multiplexing benefits of a greater antenna count.

Notably, IALMO outperforms CCPA in terms of sum rate across a wide range of numbers of antennas. For example, with $M = 12$, it delivers an $4.2\,\%$ sum rate gain over the CCPA. The SCA approximation and the rank-one SDR relaxation used in the CCPA may be the cause.

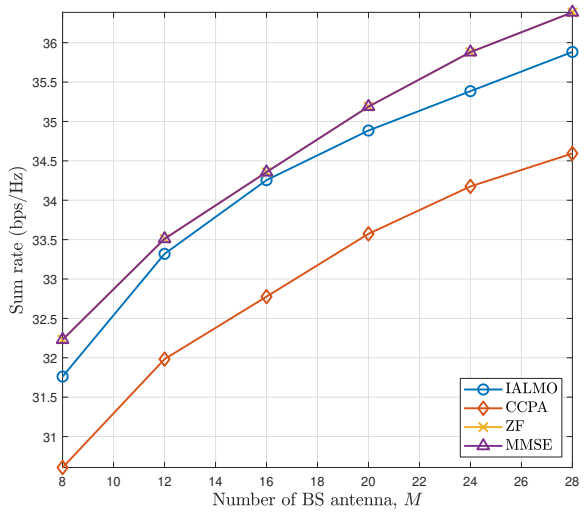

Fig. 11: Sum rate versus the number of BS antennas, M, for various algorithms.

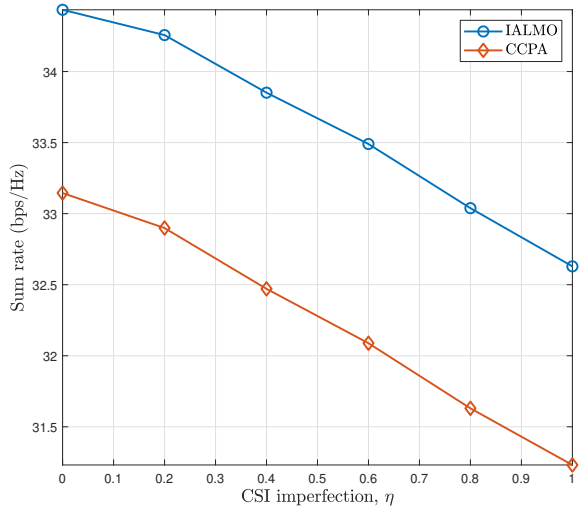

Fig. 12: Sum rate as a function of CSI imperfection, η.

I. CSI Impairments

CSI imperfections/errors can reduce wireless network performance and reliability, affecting signal reception and beamforming [54]. To this end, Fig. 12 investigates how CSI errors affect the IALMO and CCPA algorithms. The real channel x is modeled as $\tilde{x} = x + e$, $x \in \{h_{mk}\}$ for $m \in \{1, \ldots, M\}$, $\tilde{x}$ is the estimated channel, and e denotes estimation noise distributed as $e \sim \mathcal{N}(0, \sigma_e^2)$ [54], [55]. The error variance is a critical parameter that accounts for the channel estimation quality [54], [55]. It is modeled as $\sigma_e^2 = \eta |x|^2$, where $|x|$ is the magnitude of the true channel value and $0 \leq \eta \leq 1$. Thus, η is a measure of CSI error magnitude.

Fig. 12 plots the sum rate as a function of the CSI imperfection, η. Notably, both methods attain the maximum sum rate with better CSI estimation, i.e., perfect CSI with $\eta \to 0$. As η approaches 1, the sum rate attained by both the IALMO and CCPA algorithms decreases due to the impact of imperfect channels, i.e., the mismatch between the actual and estimated channels. Thus, increasing CSI imperfections lowers the communication sum rate in ISAC systems.

VIII. Conclusion

While highly touted for emerging 6G wireless, ISAC systems face non-convex resource optimization challenges. Prior solutions rely on classical algorithms and approximations, which may not yield optimal results. To address this, we introduce an algorithm based on Riemannian MO optimization and the augmented Lagrangian method (ALM), leveraging the geometric features of the solution space to deliver excellent performance. Our approach concurrently optimizes the communication sum rate while meeting SINR and sensing gain targets. The IALMO outperforms the state-of-the-art CCPA with lower computational complexity and reduced time requirements. Simulation results demonstrate its robustness and adaptability, indicating practical viability in ISAC systems. Future research directions include exploring scalability and applicability across diverse ISAC architectures to enhance efficiency and suitability for real-world deployment. Additionally, incorporating robust beamforming design can improve system reliability by addressing channel estimation errors and ensuring performance under uncertain conditions.

References

[1] A. Liu *et al.*, "A survey on fundamental limits of integrated sensing and communication," *IEEE Commun. Surveys Tuts.*, vol. 24, no. 2, pp. 994–1034, 2th Quart. 2022.

[2] J. Wang *et al.*, "Integrated sensing and communication: Enabling techniques, applications, tools and data sets, standardization, and future directions," *IEEE Internet Things J.*, vol. 9, no. 23, pp. 23 416–23 440, Dec. 2022.

[3] J. A. Zhang *et al.*, "Enabling joint communication and radar sensing in mobile networks — A survey," *IEEE Commun. Surveys Tuts.*, vol. 24, no. 1, pp. 306–345, 1st Quart. 2022.

[4] A. Hakimi, D. Galappaththige, and C. Tellambura, "A roadmap for NF-ISAC in 6G: A comprehensive overview and tutorial," *Entropy*, vol. 26, no. 9, Sept. 2024.

[5] D. Galappaththige, S. Zargari, C. Tellambura, and G. Y. Li, "Near-field ISAC: Beamforming for multi-target detection," *IEEE Wireless Communications Letters*, vol. 13, no. 7, pp. 1938–1942, Jul. 2024.

[6] X. Liu *et al.*, "Joint transmit beamforming for multiuser MIMO communications and MIMO radar," *IEEE Trans. Signal Process.*, vol. 68, pp. 3929–3944, Jul. 2020.

[7] Z. He, W. Xu, H. Shen, Y. Huang, and H. Xiao, "Energy efficient beamforming optimization for integrated sensing and communication," *IEEE Wireless Commun. Lett.*, vol. 11, no. 7, pp. 1374–1378, Jul. 2022.

[8] N. Zhao, Y. Wang, Z. Zhang, Q. Chang, and Y. Shen, "Joint transmit and receive beamforming design for integrated sensing and communication," *IEEE Commun. Lett.*, vol. 26, no. 3, pp. 662–666, Mar. 2022.

[9] H. Hua, J. Xu, and T. X. Han, "Optimal transmit beamforming for integrated sensing and communication," *IEEE Trans. Veh. Technol.*, vol. 72, no. 8, pp. 10 588–10 603, Mar. 2023.

[10] Z. He *et al.*, "Full-duplex communication for ISAC: Joint beamforming and power optimization," *IEEE J. Sel. Areas Commun.*, vol. 41, no. 9, pp. 2920–2936, Sept. 2023.

[11] D. Xu, X. Yu, D. W. K. Ng, A. Schmeink, and R. Schober, "Robust and secure resource allocation for ISAC systems: A novel optimization framework for variable-length snapshots," *IEEE Trans. Commun.*, vol. 70, no. 12, pp. 8196–8214, Dec. 2022.

[12] K. Zhong, D. An, R. Jiang, J. Hu, and C. Pan, "RIS-aided ISAC waveform design via parallel product complex circle manifold," in *Proc. IEEE Global Commun. Conf. (GLOBECOM)*, Dec. 2023, pp. 6499–6504.

[13] B. Wang, Z. Cheng, and Z. He, "Manifold optimization for hybrid beamforming in dual-function radar-communication system," *Multidimensional Syst. Signal Process.*, vol. 34, no. 1, p. 1–24, Sept. 2022.

[14] E. Shtaiwi *et al.*, "Sum-rate maximization for RIS-assisted integrated sensing and communication systems with manifold optimization," *IEEE Trans. Commun.*, vol. 71, no. 8, pp. 4909–4923, Aug. 2023.

[15] D. An *et al.*, "Robust transceiver design for ISAC systems via product complex circle-sphere manifold method," *IEEE Trans. Instrum. Meas.*, vol. 73, pp. 1–14, Feb. 2024.

[16] Z.-q. Luo, W.-k. Ma, A. M.-c. So, Y. Ye, and S. Zhang, "Semidefinite relaxation of quadratic optimization problems," *IEEE Signal Process. Mag.*, vol. 27, no. 3, pp. 20–34, May 2010.

[17] O. Mehanna, K. Huang, B. Gopalakrishnan, A. Konar, and N. D. Sidiropoulos, "Feasible point pursuit and successive approximation of non-convex QCQPs," *IEEE Signal Process. Lett.*, vol. 22, no. 7, pp. 804–808, Jul. 2015.

[18] S. Boyd and L. Vandenberghe, *Convex Optimization*. Cambridge, U.K.: Cambridge Univ. Press, 2004.

[19] Z.-Q. Luo and P. Tseng, "On the convergence of the coordinate descent method for convex differentiable minimization," *J. Optim. Theory Appl.*, vol. 72, no. 1, pp. 7–35, Jan. 1992.

[20] J. Hu, X. Liu, Z.-W. Wen, and Y.-X. Yuan, "A brief introduction to manifold optimization," *J. Oper. Res. Soc. China.*, vol. 8, pp. 199–248, Apr. 2020.

[21] N. Boumal, *An Introduction to Optimization on Smooth Manifolds*. Cambridge Univ. Press, 2023.

[22] J. M. Lee, *Riemannian Manifolds: An Introduction to Curvature*. Springer Science & Business Media, 2006, vol. 176.

[23] L. Zhou, L. Zheng, X. Wang, W. Jiang, and W. Luo, "Coordinated multicell multicast beamforming based on manifold optimization," *IEEE Commun. Lett.*, vol. 21, no. 7, pp. 1673–1676, Jul. 2017.

[24] G. Zhu, L. Chen, and K. Huang, "MIMO over-the-air computation: Beamforming optimization on the Grassmann manifold," in *Proc. IEEE Global Commun. Conf. (GLOBECOM)*, Dec. 2018, pp. 1–6.

[25] K. Zhong, J. Hu, C. Pan, X. Yu, and X. Li, "MIMO radar beampattern design based on manifold optimization method," *IEEE Commun. Lett.*, vol. 26, no. 5, pp. 1086–1090, May 2022.

[26] W. Xiong, J. Hu, and K. Zhong, "MIMO radar transmit beampattern matching via manifold optimization," in *Proc. IEEE Int. Conf. Acoust., Speech, Signal Process. (ICASSP)*, Jun. 2023, pp. 1–5.

[27] Y. Zhai, X. Li, J. Hu, and K. Zhong, "The transmit beampattern design in MIMO radar system: A manifold optimization based method," in *Proc. IEEE Radar Conf. (RadarConf22)*, Mar. 2022, pp. 1–5.

[28] C. Liu and N. Boumal, "Simple algorithms for optimization on Riemannian manifolds with constraints," *Appl. Math. Optim.*, vol. 82, pp. 949–981, Mar. 2020.

[29] X. Yu, D. Xu, and R. Schober, "MISO wireless communication systems via intelligent reflecting surfaces: (invited paper)," in *Proc. IEEE/CIC Int. Conf. Commun. (ICCC)*, Aug. 2019, pp. 735–740.

[30] R. Liu *et al.*, "Integrated sensing and communication based outdoor multi-target detection, tracking, and localization in practical 5G networks," *Intell. converg. netw.*, vol. 4, no. 3, pp. 261–272, Aug. 2023.

[31] K. Ji, Q. Zhang, Z. Wei, Z. Feng, and P. Zhang, "Networking based ISAC hardware testbed and performance evaluation," *IEEE Commun. Mag.*, vol. 61, no. 5, pp. 76–82, May 2023.

[32] X. Cheng, D. Duan, S. Gao, and L. Yang, "Integrated sensing and communications (ISAC) for vehicular communication networks (VCN)," *IEEE Internet Things J.*, vol. 9, no. 23, pp. 23 441–23 451, Dec. 2022.

[33] C. G. Tsinos, A. Arora, S. Chatzinotas, and B. Ottersten, "Joint transmit waveform and receive filter design for dual-function radar-communication systems," *IEEE J. Sel. Topics Signal Process.*, vol. 15, no. 6, pp. 1378–1392, Nov. 2021.

[34] L. Wu, P. Babu, and D. P. Palomar, "Transmit waveform/receive filter design for MIMO radar with multiple waveform constraints," *IEEE Trans. Signal Process.*, vol. 66, no. 6, pp. 1526–1540, Mar. 2018.

[35] "Positioning techniques for mobile devices in LTE," Jul. 2015. Available Online: https://www.hsc.com/resources/blog/positioning-techniques-for-mobile-devices-in-lte/.

[36] T. L. Marzetta, E. G. Larsson, H. Yang, and H. Q. Ngo, *Fundamentals of Massive MIMO*. Cambridge Univ. Press, 2016.

[37] E. Nayebi and B. D. Rao, "Semi-blind channel estimation for multiuser massive MIMO systems," *IEEE Trans. Signal Process.*, vol. 66, no. 2, pp. 540–553, Jan. 2018.

[38] Z. Wang, Y. Liu, X. Mu, Z. Ding, and O. A. Dobre, "NOMA empowered integrated sensing and communication," *IEEE Commun. Lett.*, vol. 26, no. 3, pp. 677–681, Mar. 2022.

[39] Z. Huang *et al.*, "Joint pilot optimization, target detection and channel estimation for integrated sensing and communication systems," *IEEE Trans. Wireless Commun.*, vol. 21, no. 12, pp. 10 351–10 365, Dec. 2022.

[40] Z. Xiao and Y. Zeng, "Full-duplex integrated sensing and communication: Waveform design and performance analysis," in *Proc. 13th Int. Conf. Wireless Commun. Signal Process. (WCSP)*, Oct. 2021, pp. 1–5.

[41] M. A. Richards, J. A. Scheer, and W. A. Holm, Eds., *Principles of Modern Radar: Basic principles*, ser. Radar, Sonar and Navigation. Inst. Eng. Technol., 2010.

[42] P. Stoica, J. Li, and Y. Xie, "On probing signal design for MIMO radar," *IEEE Trans. Signal Process.*, vol. 55, no. 8, pp. 4151–4161, Jul. 2007.

[43] B. Tang and J. Li, "Spectrally constrained MIMO radar waveform design based on mutual information," *IEEE Trans. Signal Process.*, vol. 67, no. 3, pp. 821–834, Feb. 2019.

[44] D. Galappaththige, C. Tellambura, and A. Maaref, "Integrated sensing and backscatter communication," *IEEE Wireless Commun. Lett.*, vol. 12, no. 12, pp. 2043–2047, Dec. 2023.

[45] S. Zargari, A. Khalili, and R. Zhang, "Energy efficiency maximization via joint active and passive beamforming design for multiuser MISO IRS-aided SWIPT," *IEEE Wireless Commun. Lett.*, vol. 10, no. 3, pp. 557–561, Mar. 2021.

[46] K. Shen and W. Yu, "Fractional programming for communication systems—part II: Uplink scheduling via matching," *IEEE Trans. Signal Process.*, vol. 66, no. 10, pp. 2631–2644, May 2018.

[47] ——, "Fractional programming for communication systems—part I: Power control and beamforming," *IEEE Trans. Signal Process.*, vol. 66, no. 10, pp. 2616–2630, May 2018.

[48] E. G. Birgin and J. M. Martínez, *Practical Augmented Lagrangian Methods for Constrained Optimization*. Philadelphia, PA: Soc. Ind. Appl. Math., 2014.

[49] P.-A. Absil, R. Mahony, and R. Sepulchre, *Optimization Algorithms on Matrix Manifolds*. Princeton, NJ, USA: Princeton Univ. Press, 2009.

[50] J. R. Shewchuk, "An introduction to the conjugate gradient method without the agonizing pain," USA, Tech. Rep., 1994. [Online]. Available: http://www.cs.cmu.edu/ quake-papers/painless-conjugate-gradient.pdf

[51] E. G. Birgin, C. A. Floudas, and J. M. Martínez, "Global minimization using an augmented Lagrangian method with variable lower-level constraints," *Math. Program.*, vol. 125, no. 1, pp. 139–162, Jan. 2010.

[52] R. G. Bartle and D. R. Sherbert, *Introduction to Real Analysis*. Wiley New York, 2000, vol. 2.

[53] Q. Wu and R. Zhang, "Intelligent reflecting surface enhanced wireless network via joint active and passive beamforming," *IEEE Trans. Wireless Commun.*, vol. 18, no. 11, pp. 5394–5409, Nov. 2019.

[54] S. Zhou and G. Giannakis, "How accurate channel prediction needs to be for transmit-beamforming with adaptive modulation over Rayleigh MIMO channels?" *IEEE Trans. Wireless Commun.*, vol. 3, no. 4, pp. 1285–1294, Jul. 2004.

[55] S. M. Kay, *Fundamentals of Statistical Signal Processing: Estimation Theory*. USA: Prentice-Hall, Inc., 1993.

Shayan Zargari received the B.Sc. degree in Electronic Engineering from Azad University, South Tehran Branch, Tehran, Iran, in 2018, and the M.Sc. degree in Telecommunication Engineering from the Iran University of Science and Technology, Tehran, Iran, in 2020. He is currently pursuing the Ph.D. degree in communications and signal processing at the University of Alberta, Edmonton, AB, Canada.

From 2019 to 2020, he was a visiting researcher at the Electronics Research Institute, Sharif University of Technology, Tehran, Iran, and from 2020 to 2021, he was a visiting researcher at the Department of Electrical and Computer Engineering, Tarbiat Modares University, Tehran, Iran. His research interests include optimization theory, integrated sensing and communication (ISAC), backscatter communication (BackCom), intelligent reflecting surfaces (IRS), unmanned aerial vehicle (UAV) communications, resource allocation in fifth-generation (5G)/six-generation (6G) wireless communication, and green communication. He serves as a reviewer for several IEEE journals, including IEEE JOURNAL ON SELECTED AREAS IN COMMUNICATIONS, IEEE TRANSACTIONS ON COMMUNICATIONS, and IEEE TRANSACTIONS ON WIRELESS COMMUNICATIONS.

Diluka Galappaththige (S'17, M'22) is a postdoctoral research fellow at the Department of Electrical and Computer Engineering, University of Alberta, Canada. He received his B.Sc. degree (First-class honor) in Electrical and Electronic Engineering from the Department of Electrical and Electronic Engineering, University of Peradeniya, Sri Lanka, in 2017, and his Ph.D. in Electrical and Computer Engineering from the School of Electrical, Computer, and Biomedical Engineering, Southern Illinois University, Carbondale, IL, USA, in 2021.

Dr. Galappaththige has been awarded a post-doctoral fellowship from NSERC for the academic year 2024-2026. His current research interests include but are not limited to, the design, modeling, and analysis of massive multiple-input multiple-output (mMIMO) communication (i.e., including co-located mMIMO and cell-free/distributed mMIMO), full-duplex communication (FD), backscatter communication (BackCom), reconfigurable intelligent surfaces (RISs), integrated sensing and communication (ISAC), near-filed ISAC, wireless power transfer, and emerging technologies for enabling fifth-generation (5G) and beyond wireless networks. He was a recipient of the Exemplary Reviewer Award for IEEE Wireless Communications Letters (TWCL) in 2020, and IEEE Communications Letters (TCL) in 2021. He has actively served as a reviewer for a variety of IEEE journals and conferences, including IEEE Transactions on Communications, IEEE Internet of Things Journal, IEEE Transactions on Vehicular Technology, IEEE Transactions on Green Communications and Networking, IEEE Access, IEEE Network, IEEE Open Journal of Communications Society, TCL, TWCL, IEEE International Conference on Communications, and IEEE Global Communications Conference.

Chintha Tellambura (Fellow, IEEE) received the B.Sc. degree (First class) in electrical and electronic engineering from the University of Moratuwa, Sri Lanka, the M.Sc. degree in electrical engineering from King's College, University of London, and the Ph.D. degree in electrical engineering from the University of Victoria, Canada. He was with Monash University, Australia, from 1997 to 2002. Dr. Tellambura is a Professor in the Department of Electrical and Computer Engineering at the University of Alberta. He has authored or co-authored over 650 journals and conference papers, demonstrating his expertise in the field. According to Google Scholar, his exceptional scholarly contributions have earned him an impressive H-index of 84. Dr. Tellambura has made significant contributions to various areas of research, including future wireless networks, machine learning for wireless networks, and signal processing.

Recognizing his outstanding accomplishments, he was elected as an IEEE Fellow in 2011 for his noteworthy contributions to physical layer wireless communication theory. In 2017, he was further honored as a fellow of the Canadian Academy of Engineering, a testament to his exceptional achievements. His dedication and expertise have been acknowledged through prestigious awards, including the Best Paper Awards in the Communication Theory Symposium in 2012, the IEEE International Conference on Communications (ICC) held in Canada in 2017, and another ICC in France. Moreover, Dr. Tellambura has been honored with the esteemed McCalla Professorship and the Killam Annual Professorship by the University of Alberta, further underscoring his significant impact on academia. Dr. Tellambura has also played a vital role in editorial responsibilities within the IEEE community. He served as an Editor for the IEEE Transactions on Communications from 1999 to 2011 and for the IEEE Transactions on Wireless Communications from 2001 to 2007. In the latter role, he was Area Editor of Wireless Communications Systems and Theory from 2007 to 2012, contributing to advancing the field through his editorial expertise.

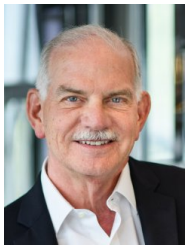

H. Vincent Poor (S'72, M'77, SM'82, F'87) received the Ph.D. degree in EECS from Princeton University in 1977. From 1977 until 1990, he was on the faculty of the University of Illinois at Urbana-Champaign. Since 1990 he has been on the faculty at Princeton, where he is currently the Michael Henry Strater University Professor. During 2006 to 2016, he served as the dean of Princeton's School of Engineering and Applied Science, and he has also held visiting appointments at several other universities, including most recently at Berkeley and Caltech. His research interests are in the areas of information theory, machine learning and network science, and their applications in wireless networks, energy systems and related fields. Among his publications in these areas is the book *Machine Learning and Wireless Communications*. (Cambridge University Press, 2022). Dr. Poor is a member of the National Academy of Engineering and the National Academy of Sciences and is a foreign member of the Royal Society and other national and international academies. He received the IEEE Alexander Graham Bell Medal in 2017.